Isolating the Evolving Contributions of Anthropogenic Aerosols and Greenhouse Gases: A New CESM1 Large Ensemble Community Resource

CLARA DESER, ADAM S. PHILLIPS, ISLA R. SIMPSON, NAN ROSENBLOOM, DANI COLEMAN,
FLAVIO LEHNER, AND ANGELINE G. PENDERGRASS

Climate and Global Dynamics Division, NCAR, Boulder, Colorado

PEDRO DINEZIO

The University of Texas at Austin, Austin, Texas

SAMANTHA STEVENSON

University of California at Santa Barbara, Santa Barbara, California

ABSTRACT

The evolving roles of anthropogenic aerosols (AER) and greenhouse gases (GHG) in driving large-scale patterns of precipitation and SST trends during 1920–2080 are studied using a new set of "all-but-one-forcing" initial-condition large ensembles (LEs) with the Community Earth System Model version 1 (CESM1), which complement the original "all-forcing" CESM1 LE (ALL). The large number of ensemble members (15–20) in each of the new LEs enables regional impacts of AER and GHG to be isolated from the noise of the model's internal variability. Our analysis approach, based on running 50-yr trends, accommodates geographical and temporal changes in patterns of forcing and response. AER are shown to be the primary driver of large-scale patterns of externally forced trends in ALL before the late 1970s, and GHG to dominate thereafter. The AER and GHG forced trends are spatially distinct except during the 1970s transition phase when aerosol changes are mainly confined to lower latitudes. The transition phase is also characterized by a relative minimum in the amplitude of forced trend patterns in ALL, due to a combination of reduced AER and partially offsetting effects of AER and GHG. Internal variability greatly limits the detectability of AER- and GHG-forced trend patterns in individual realizations based on pattern correlation metrics, especially during the historical period, highlighting the need for LEs. We estimate that <20% of the spatial variances of observed precipitation and SST trends are attributable to AER and GHG forcing, although model biases in patterns of forced response and signal-to-noise may affect this estimate.

1. Introduction

Anthropogenic aerosols (AER) and greenhouse gases (GHG) are the dominant drivers of forced climate change on a global scale over the past century, with opposing effects on the planetary radiative energy balance (Myhre et al. 2013; Zhao et al. 2019). AER cause a net cooling through increased absorption and scattering of shortwave radiation (direct effects) and changes in cloud microphysical properties (indirect effects, also referred to as aerosol–cloud interactions) [see the recent review by Bellouin et al. (2020)], while GHG induce warming through enhanced absorption of longwave radiation. AER and GHG differ not only in their radiative impacts, but also in their geographical distributions and temporal evolutions. AER are spatially heterogeneous, originating primarily over the major industrial centers of the Northern Hemisphere (NH) and Southeast Asia, with additional sources from biomass burning, while GHG are globally predominantly well mixed. Temporal changes in AER are regionally

Corresponding author: Dr. Clara Deser, cdeser@ucar.edu

specific, whereas GHG concentrations have risen approximately monotonically in all locations. For example, AER over North America and western Europe increased rapidly from the 1940s to 1970s followed by a gradual decline, while those over Southeast Asia have risen continuously since the late 1940s (Lamarque et al. 2010; Stevens 2015; Persad and Caldeira 2018; Samset et al. 2019). These contrasting aspects of AER and GHG complicate the study of anthropogenic climate change on regional scales, including physical understanding, detection and attribution, and model projections. In addition, the magnitude of AER forcing remains uncertain (Wilcox et al. 2015; Samset et al. 2019; Wilcox et al. 2020; Bellouin et al. 2020).

The physical mechanisms underpinning the large-scale response of the climate system to radiative perturbations associated with AER and GHG have been investigated using a range of approaches, including theoretical considerations, simplified modeling experiments with idealized forcings, and full complexity Earth system model (ESM) simulations with realistic radiative forcing scenarios. Collectively, these approaches have led to the following insights and understanding. On a global scale, energetic constraints dictate that enhanced NH cooling induced by AER sources in Eurasia and North America will cause an interhemispheric climate shift, including a southward displacement of the zonal-mean intertropical convergence zone (ITCZ) (e.g., Rotstayn and Lohmann 2002; Ming and Ramaswamy 2009; Hwang et al. 2013; Wang et al. 2016; Chung and Soden 2017; Soden and Chung 2017; Wang et al. 2019). In contrast, GHG-induced global warming will produce a zonal mean response that is largely symmetric about the equator, with additional asymmetries introduced by the mean state and continental configuration. In general, the zonal-mean response to GHG is characterized by enhanced rainfall in the deep tropics and drying in the subtropics, following the "wet-get-wetter" and "upped ante" paradigms (e.g., Held and Soden 2006; Xie et al. 2010, 2013; Wang et al. 2016; Neelin et al. 2003). The zonal-mean responses to both AER and GHG are strongly mediated by dynamical ocean–atmosphere interactions, in particular oceanic meridional heat transports associated with the wind-driven subtropical overturning cells and the Atlantic meridional overturning circulation (Kang et al. 2018, 2019; Tomas et al. 2016; Wang et al. 2018). In addition, both types of radiative forcing induce amplified temperature (and associated precipitation) responses in the Arctic as a result of positive ice-albedo feedback (Deng et al. 2020; Zhao et al. 2019).

Regional aspects of the precipitation and sea surface temperature (SST) responses to AER and GHG changes have been widely studied. These include impacts on Sahel rainfall (e.g., Haywood et al. 2013; Dong et al. 2014; Giannini and Kaplan 2019; Hirasawa et al. 2020, manuscript submitted to *J. Climate*, the Asian monsoon (Ganguly et al. 2012; Undorf et al. 2018a; Li et al. 2018; Zhao et al. 2019), Eurasian climate (Undorf et al. 2018b), and regional patterns of SST change (Xie et al. 2010, 2013; Wang et al. 2016). Air–sea interactions are important modulators of these responses, with both thermodynamic and dynamic processes contributing (Li et al. 2018; Kang et al. 2018, 2019). For example, the wind–evaporation–SST (WES) feedback mechanism, SST–cloud interactions, and wind-driven changes in ocean gyre-scale circulations contribute to the formation of regional patterns of SST response (Xie et al. 2010). These air–sea feedback mechanisms operate under both AER and GHG forcing, and thus impart a degree of commonality to the regional patterns of SST response to AER and GHG changes (Xie et al. 2013). Aerosol–cloud interactions also play an important role in the response of the climate system to AER forcing (Chung and Soden 2017; Soden and Chung 2017), with impacts on climate feedbacks and climate sensitivity (Gettelman et al. 2016; Ghan et al. 2016; Gryspeerdt et al. 2020).

A majority of the studies cited above adopt a "time slice" approach to their analysis of climate model simulations by contrasting two different periods, for example preindustrial vs. present-day (e.g., Li et al. 2018; Chung and Soden 2017; Soden and Chung 2017; Deng et al. 2020), early vs. late twentieth century (Hwang et al. 2013), 1970s vs. 2010s (Zhao et al. 2019), and present-day vs. late twenty-first century (Xu et al. 2018). Others prescribe idealized time-invariant radiative perturbations in a hierarchy of models to probe dependencies upon amplitude, geographical location, and degree of air–sea coupling (Seo et al. 2014; Persad and Caldeira 2018; White et al. 2018; Kang et al. 2018, 2019). One recent multimodel ensemble compared two different greenhouse gas and two different aerosol forcings (Myhre et al. 2017). Such idealized and time-slice approaches are fruitful for establishing a mechanistic understanding of the response to a particular configuration of radiative forcing, which may or may not lend itself to "pattern scaling" for future projections (Tebaldi and Arblaster 2014; Pendergrass et al. 2015). However, by design, these studies do not take into account the full complexity of the observed spatiotemporal evolution of AER over the historical period, nor do they consider how the changing geographical distribution of AER may interact with rising GHGs as a function of time, nor to what extent the evolving forced responses may be obscured by multi-decadal trends driven by internal variability. Nonlinear interactions between AER and GHG were investigated in Gettelman et al. (2016), Deng et al. (2020), and Zhao et al. (2019), but only for a particular time period.

Apart from the idealized modeling studies, the majority of aforementioned studies were based on a limited collection of "single forcing" AER and GHG historical simulations conducted with a subset of models participating in phase 5 of the Coupled Model Intercomparison Project (CMIP5; Taylor et al. 2012). Because of the limited number (1–5) of simulations for each of the eight models in this single-forcing archive, the analyses relied on the multimodel mean to estimate the forced response. However, averaging across models confounds model structural uncertainty and uncertainty due to internal variability (i.e., Hawkins and Sutton 2009; Deser et al. 2012). This may be particularly problematic in the case of AER, since each model differs in its representation of aerosol direct and indirect effects (e.g., Zelinka et al. 2014; Bellouin et al. 2020). In addition, structural uncertainty may be an issue for responses that are closely tied to the mean state, as is the case for tropical precipitation (Xie et al. 2010).

To circumvent the issue of structural uncertainty, initial-condition large ensembles (LEs) have been used to determine the forced response in a given climate model (e.g., Deser et al. 2020). In such a LE, each simulation is conducted with the same model and radiative forcing scenario but begins from a different initial state; thus, ensemble spread is solely attributable to unpredictable internal variability and the forced response can be estimated from the ensemble mean (e.g., Deser et al. 2012; Kay et al. 2015; Maher et al. 2019; Lehner et al. 2020). Almost all LEs to date prescribe the full suite of anthropogenic and natural radiative forcing factors (see Table 1 in Deser et al. 2020), including the widely used 40-member Community Earth System Model version 1 (CESM1) LE (Kay et al. 2015). Here, we introduce a new set of CESM1 LEs in which industrial AER, biomass burning AER, or GHG is kept fixed at 1920 conditions, while all other external anthropogenic and natural forcings evolve following those in the original "all-forcing" CESM1 LE (i.e., historical and future RCP8.5 scenarios over the period 1920–2080). These new LEs provide a unique community resource for studying the regional impacts of AER and GHG over the twentieth and twenty-first centuries. To the best of our knowledge, the only other comprehensive models with complementary historical and future all-forcing and single-forcing LEs are the Canadian ESM version 2, which begins in 1950 and also employs CMIP5 forcings (Santer et al. 2019; Bonfils et al. 2020), and the Canadian ESM version 5, which begins in 1850 and employs CMIP6 forcings (Swart et al. 2019).

The purpose of this study is to use the new set of CESM1 LEs 1) to isolate the evolving patterns of precipitation and SST response to AER and GHG forcing over the period 1920–2080; 2) to quantify as a function of time the relative contributions of AER and GHG forcing to externally driven climate trends; and 3) to assess the degree to which AER- and GHG-induced effects can be detected in a single ensemble member and observations. Our simple analysis approach, based on running 50-yr trends, accommodates temporal changes in the spatial patterns of forcing and response, an aspect that has been largely neglected in previous studies. Such a perspective is particularly advantageous for AER (and its interactions with GHG) due to pronounced changes in the geographical distribution of emissions over time. The rest of this paper is organized as follows. The model simulations, observational datasets, and analysis approach are described in section 2. Results are presented in section 3, summarized in section 4, and discussed in section 5.

2. Data and methods

a. Model simulations

All experiments use the same model version and nominal 1° spatial resolution as the 40-member fully coupled global CESM1 LE described in Kay et al. (2015). CESM1 consists of interactive atmosphere, ocean, land, and sea ice component models, as well as a terrestrial carbon cycle, and diagnostic biogeochemistry calculations for the ocean ecosystem and the atmospheric carbon dioxide cycle, which do not feed back on the model's physical climate. The atmospheric model component is Community Atmosphere Model version 5 (CAM5; Neale et al. 2012), which includes a three-mode modal aerosol scheme (Liu et al. 2012) with prognostic aerosols and indirect effects (aerosol–cloud interactions) for both liquid and ice phase clouds in the "stratiform regime" (Morrison and Gettelman 2008; Gettelman et al. 2010). CESM1 has a present-day value of aerosol effective radiative forcing of $-1.37\,\mathrm{W\,m^{-2}}$ (Zelinka et al. 2014), which falls within the one standard deviation range of plausible estimates (from -1.6 to $-0.6\,\mathrm{W\,m^{-2}}$; Bellouin et al. 2020). The 40-member CESM1 LE (Kay et al. 2015) is configured as follows. The first ensemble member begins in 1850 from year 401 of a long preindustrial control simulation, and is integrated forward under historical (prior to 2006) and future (RCP8.5 for 2006–2100) emissions scenarios. All other members are branched from the first member in 1920 and are subject to the same forcing protocol, but differ by a small (order $10^{-14}\,\mathrm{K}$, the level of "round-off" error in CAM5) random noise perturbation to their initial atmospheric temperature fields. The CESM1 "all forcing" LE (hereafter referred to as "ALL") realistically simulates the evolution of global-mean surface air

temperature (GMST) during 1920–2019, with observations lying within the ensemble spread nearly every year (Fig. 1a). The observed linear trend in GMST during this period [0.89°C (100 yr)$^{-1}$] is also within the ensemble spread [0.64°–0.95°C (100 yr)$^{-1}$].

The new set of CESM1 LEs conducted for this study use the same forcing protocol as ALL, except that one forcing agent is held fixed at 1920 conditions as follows: 1) a 20-member ensemble with fixed GHGs (hereafter "XGHG"); 2) a 20-member ensemble with fixed industrial AER (hereafter "XAERindus"); and 3) a 15-member ensemble with fixed biomass-burning AER (hereafter "XAERbmb"). Each member of the "X" ensembles begins from the same state as the first member of ALL in 1920 and is initialized in the same manner as described above for ALL. The XAERindus and XGHG ensembles end in 2080, while the XAERbmb ends in 2030 (note that biomass-burning aerosols in RCP8.5 do not change appreciably after 2030).

To determine the effect of the forcing factor that was held fixed in the "X" ensembles, we subtract the ensemble mean of the "X" ensemble from the ensemble mean of ALL and term these residuals AERindus, AERbmb, and GHG. Note that these residuals include any nonlinear interactions among AERindus, AERbmb, and GHG that are present in ALL. For example, AERindus may interact nonlinearly with GHG in the ALL ensemble, but this interaction is absent in XAERindus. The conversions from XAERindus to AERindus, and from XGHG to GHG, are illustrated for GMST in Figs. 1b and 1c (the effect of AERbmb on GMST is negligible; not shown). GMST in XGHG (red curve and pink shading, Fig. 1b) decreases by approximately 0.5°C from about 1940–90, while in XAERindus (blue curve and shading, Fig. 1b) it increases by approximately 1.4°C from about 1930 to the present, which is nearly 0.4°C more than the increase in ALL (black curve and gray shading, Fig. 1b). Synchronous episodic cooling associated with volcanic eruptions in 1963, 1982, and 1991 is evident in all three records. The GMST time series in GHG (red curve and pink shading, Fig. 1c) is very similar to that in XAERindus, and GMST in AERindus (blue curve and shading, Fig. 1c) is very similar to that in XGHG except for the lack of volcanic signatures. This close resemblance attests to the dominant influence of AERindus and GHG on ensemble-mean GMST compared to other anthropogenic and natural forcings (with the notable exception of volcanic eruptions).

The combined effects of internal variability and forced response in any individual member of the GHG, AERindus, and AERbmb ensembles can be calculated as follows:
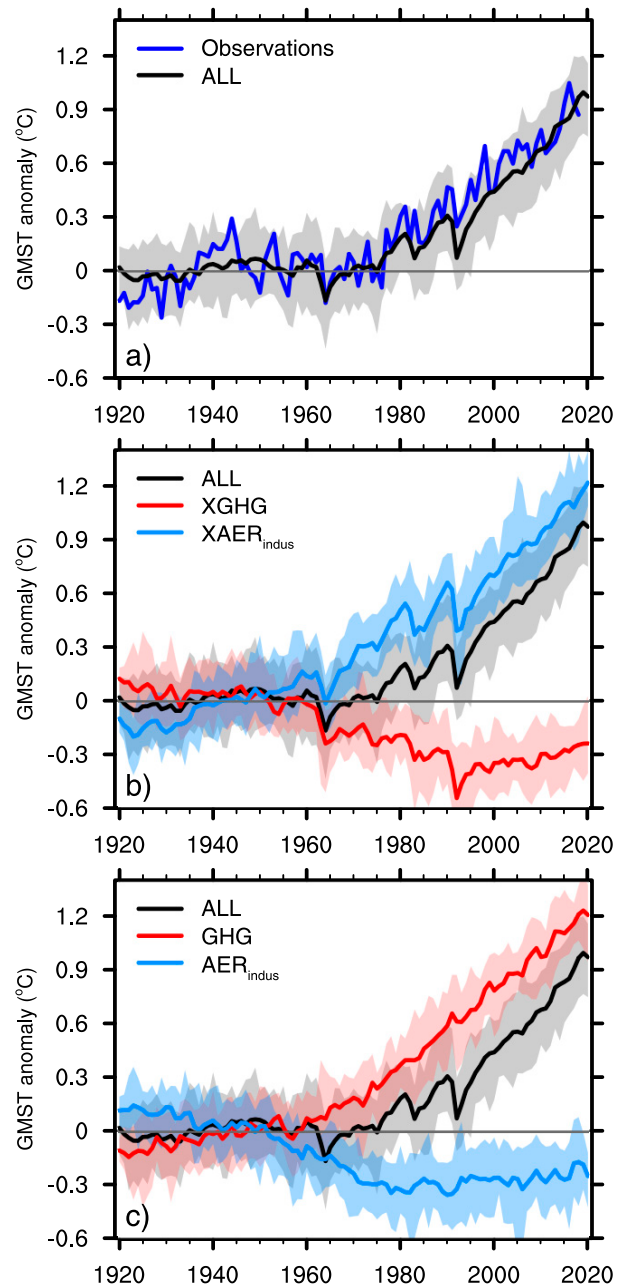

FIG. 1. Time series of annual global-mean surface air temperature (GMST) anomalies (°C) during 1920–2020 in (a) CESM1 ALL (black curve shows the ensemble mean and gray shading shows the ensemble spread) and observations (1920–2019 from Berkeley Earth Surface Temperature; Rohde et al. 2013; blue curve); (b) CESM1 ALL (black curve and gray shading), CESM1 XGHG (red curve and pink shading), and CESM1 XAERindus (light blue curve and shading); and (c) CESM1 ALL (black curve and gray shading), GHG (red curve and pink shading), and AERindus (light blue curve and shading). Anomalies are defined relative to the 1920–70 long-term means. See text for details.

$$GHG_i = XGHG_i - 2XGHG_{em} + ALL_{em}, \qquad (1)$$

$$AERindus_i = XAERindus_i - 2XAERindus_{em} + ALL_{em}, \qquad (2)$$

$$AERbmb_i = XAERbmb_i - 2XAERbmb_{em} + ALL_{em}, \qquad (3)$$

where the subscript "*i*" refers to an individual ensemble member, and the subscript "em" refers to the ensemble mean. These equations follow from the definition of internal variability in member *i* of the "X" ensemble (i.e., $XGHG_i - XGHG_{em}$), and the definition of the response to the withheld forcing (i.e., $ALL_{em} - XGHG_{em}$). Hereafter, we focus on the combined effects of AERindus and AERbmb (termed AER) by summing their contributions. Data from the new CESM1 LEs are publicly available at http://www.cesm.ucar.edu/working_groups/ CVC/simulations/cesm1-single_forcing_le.html.

b. Observational datasets

We make use of the following observational datasets over the period 1920–2018, all at monthly resolution: 1) precipitation from the Global Precipitation Climatology Centre (GPCC) version 7, a gridded gauge-analysis product with a spatial resolution of 2.5° latitude × 2.5° longitude (Schneider et al. 2015); 2) near-surface air temperatures (SAT) from the Berkeley Earth Surface Temperature (BEST) station-based dataset at 1° spatial resolution (Rohde et al. 2013); and 3) SSTs from the NOAA Extended Reconstruction Sea Surface Temperature version 5 (ERSSTv5) dataset at 5° spatial resolution (Huang et al. 2017). We also include comparison to the Global Precipitation Climatology Product (GPCP) version 2.3 (Adler et al. 2018), which provides near-global coverage by incorporating satellite data and is available for the period 1979–2018, as well as to the Hadley Centre Sea Ice and Sea Surface Temperature (HadISST) version 1 dataset (Rayner et al. 2003).

c. Analysis methods

We compute linear trends using least squares regression analysis and assess statistical significance at the 90% confidence level using a two-tailed Student's *t* test. These trends are calculated over 50-yr periods, but our results are insensitive to small changes in trend length (i.e., 40- and 60-yr trends yield similar results). All observational data are regridded to match the spatial resolution of CESM1 using bilinear interpolation. Area weighting is used for constructing all regional and global time series, as well as for computing spatial correlation coefficients (the latter are computed after removing the spatial mean of each field). All results are based on

annual means. Henceforth, for convenience we shall use the term "historical period" to refer to the interval from 1920–2019, with the understanding that all simulations are subject to RCP8.5 forcing protocols after 2005 (recall section 2a).

3. Results

a. Evolution of aerosol optical depth

Aerosol optical depth (AOD) at a wavelength of 550 nm provides a proxy for the magnitude of AER forcing. Over the historical period (1920–2019), the ensemble mean AOD in AER shows distinctive behavior over key regions (Fig. 2). In particular, North America and Europe combined exhibit a slight increase from 1920 to 1950, followed by a rapid rise from about 1955–75 and a subsequent and similarly rapid decline to the present (Fig. 2a). In contrast, the southeastern portion of the Asian continent (hereafter referred to as "Southeast Asia" for convenience, although our usage differs from geographical convention) shows a steady increase in AOD from the 1930s until the present (Fig. 2b), while tropical South America and Africa show a pronounced rise from 1945 to 1990 and remain relatively steady thereafter (Fig. 2c).

The evolving spatial patterns of AOD changes in AER over the historical period are portrayed in Figs. 2d–f based on ensemble-mean trends for three overlapping 50-yr intervals: 1930–79, 1950–99, and 1970–2019 (these intervals, henceforth referred to respectively as "early," "middle," and "late," provide a succinct way of summarizing the evolution of slow changes in AOD during 1930–2019). Note that we omit the first 10 years of the model simulations from our analysis to guard against potential memory from the single ocean initial condition used for the LEs (Yeager et al. 2018). Consistent with the regional AOD time series, the early period shows positive AOD trends in the NH, South America, and Africa, with maximum values in the main AER source regions (Europe, Southeast Asia, and tropical Africa and South America), and slight declines in parts of the SH (Fig. 2d). The AOD increases over tropical Africa and South America are largely a result of biomass burning AER precursor emissions resulting from human interference (van Marle et al. 2017), while those over Southeast Asia, Europe, and North America are primarily due to industrial AER precursor emissions (note that biomass burning decreases offset to a large extent industrial emissions over eastern North America during this early period; see Fig. S1 in the online supplemental material). In the middle period, the main regions of AOD increase shift to the tropics, with maximum trends over Southeast Asia and weaker values over
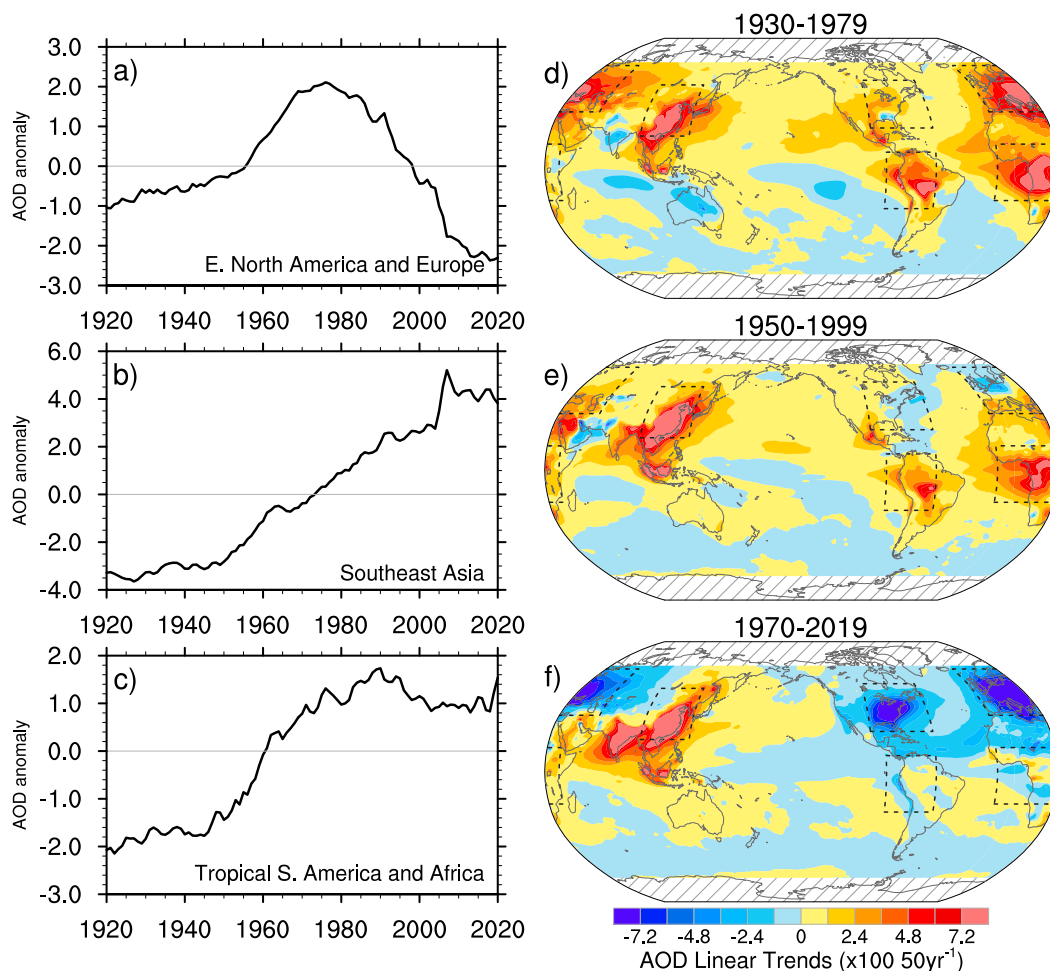
FIG. 2. Aerosol optical depth (AOD) at a wavelength of 550 nm (no units, multiplied by 100) from the AER ensemble mean. Regional anomaly time series relative to the 1920–2020 base period for (a) eastern North America and Europe, (b) Southeast Asia, and (c) tropical South America and Africa [regions identified in (d)–(f)]. Spatial distribution of linear trends in AOD during (d) 1930–79, (e) 1950–99, and (f) 1970–2019. AOD values in polar regions (hatching) are omitted for plotting purposes only.

tropical Africa and South America (Fig. 2e). The late period exhibits pronounced declines in AOD over Europe and eastern North America, and strong increases over India and Southeast Asia (Fig. 2f). The striking differences in the spatial distribution of aerosol-induced AOD trends among the three periods has important implications for the evolving large-scale patterns of SST and precipitation response discussed next.

b. Evolution of forced SST trends

In this section, we present the evolution of forced changes in SST in the AER, GHG, and ALL ensembles using the same framework of overlapping 50-yr trends as for AOD above. Global trend maps and associated zonal mean trends for each period are shown in Fig. 3; results for SAT (with coverage over ocean, land, and sea ice) are

shown in Fig. S2. During the early period (1930–79), SST trends in ALL are dominated by an interhemispheric structure, with generally negative values over the NH and positive values over the SH (Fig. 3a), consistent with the lack of an appreciable global-mean trend (recall Fig. 1a). Notable regional features include enhanced warming over the southeastern tropical Pacific and Indian Oceans, and enhanced cooling over the northwestern subtropical Pacific and subpolar North Atlantic. In the middle period (1950–99), SST trends in ALL are positive in both hemispheres (except near Nova Scotia), resulting in a more spatially homogenous pattern than the early period, although a remnant of interhemispheric asymmetry remains (more warming in the SH compared to the NH; Fig. 3b). The late period (1970–2019) in ALL is characterized by amplified warming
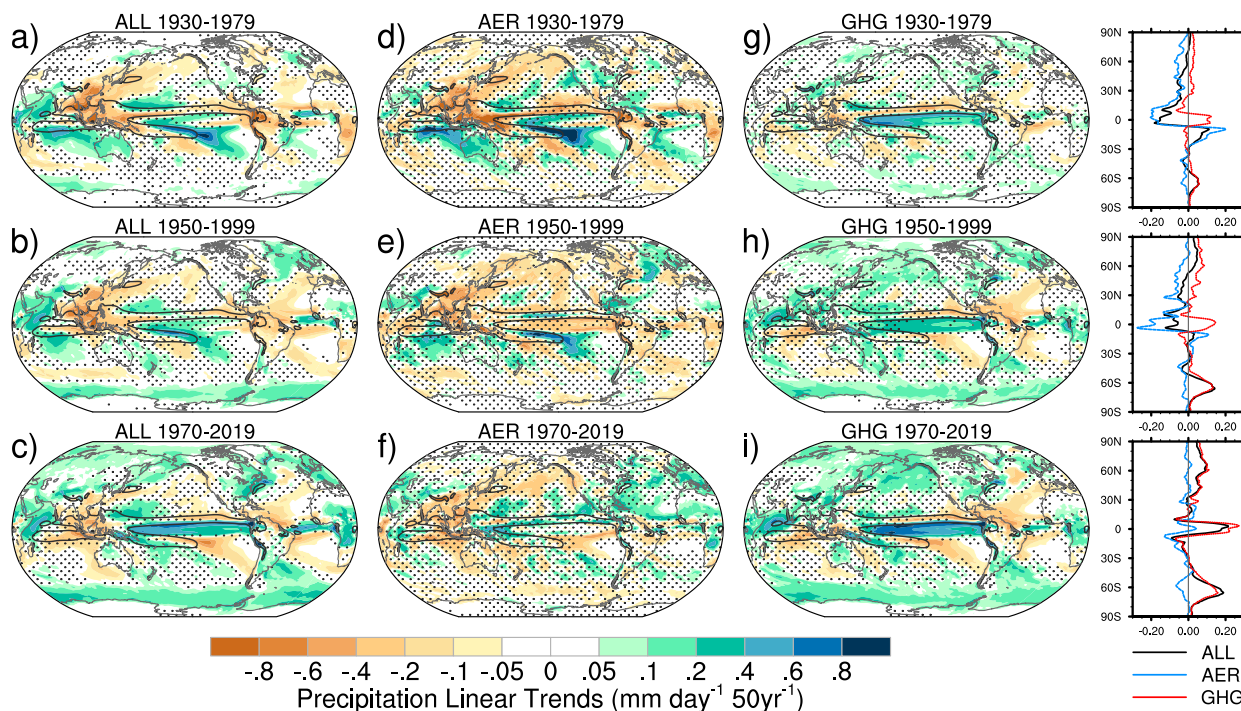
FIG. 3. Linear trends in CESM1 ensemble-mean SST [K $(50\,\mathrm{yr})^{-1}$] based on (a) ALL 1930–79; (b) ALL 1950–99; (c) ALL 1970–2019; (d) AER 1930–79; (e) AER 1950–99; (f) AER 1970–2019; (g) GHG 1930–79; (h) GHG 1950–99; and (i) GHG 1970–2019. Stippled regions indicate insignificant values at the 90% confidence level based on a two-sided t test. Gray shading at the poles denotes regions with sea ice. Panels on the right show zonal-mean profiles (60°S–65°N) of the trend maps in each row: ALL (black), AER (blue), and GHG (red).

and a large degree of equatorial symmetry (Fig. 3c). In particular, maximum warming occurs along the equator in the Pacific and Atlantic, with reduced warming over the subtropical eastern basins of both hemispheres; cooling is seen over the central subpolar North Atlantic.

The large-scale SST trend pattern driven by AER in the early period is similar to that in ALL (with some regional exceptions such as the subpolar North Atlantic), but with an overall offset due to global cooling (Fig. 3d). The spatial correlation coefficient between the SST trends in ALL and AER [denoted r(ALL, AER)] is 0.64 based on the global domain and 0.86 for the tropics (30°N–30°S). In the middle period, AER continues to cool most of the global oceans, with the most pronounced SST declines along the northern and eastern margins of the North Pacific; a localized center of warming occurs to the south of Greenland (Fig. 3e). The imprint of the AER-induced pattern is evident over the Pacific sector in ALL, but other regions such as the subpolar North Atlantic show differences [r(ALL, AER) = 0.40 global, 0.48 tropics]. In the late period, the NH cooling due to AER weakens, and is replaced by warming over the entire North Atlantic; this pattern bears little resemblance to that in ALL [r(ALL, AER) = 0.27 global, 0.37 tropics] (Fig. 3f). The reversal of

the cooling trends in the North Atlantic sector and the Mediterranean Sea in the late period is likely a result of concurrent AOD declines over North America and Europe. The localized warming of the subpolar North Atlantic, which develops in the early period and subsequently intensifies and persists, may be associated with a gradual strengthening of AMOC in response to global cooling. The decreasing resemblance between AER and ALL with time is also evident in the zonal mean trend profiles.

The pattern of GHG-induced SST trends is largely static, with an increase in magnitude over the historical period (Figs. 3g–i). This pattern consists of amplified warming over the equatorial Pacific and Atlantic, the western Indian Ocean, the North Pacific, and portions of the Southern Ocean, and cooling over the subpolar North Atlantic, consistent with previous studies (e.g., Manabe and Stouffer 1993; Xie et al. 2010; DiNezio et al. 2009). Pattern correlations between SST trends in ALL and GHG [r(ALL, GHG)] increase with time, from 0.26 and 0.24 in the early and middle periods, respectively, to 0.74 in the late period based on the global domain (similar values are found for the tropical domain: 0.24, 0.26, and 0.74, respectively). The increasing resemblance between GHG

FIG. 4. As in Fig. 3, but for precipitation [mm day^{-1} (50 yr)$^{-1}$]. The contours show the 6 mm day^{-1} isopleth of the precipitation climatology (1930–2019) from ALL.

and ALL with time is also evident in the zonal mean trend profiles.

c. Evolution of forced precipitation trends

Global trend maps and associated zonal mean trends of precipitation for each period are shown in Fig. 4 (precipitation trends as a percentage of the climatology in each period are shown in Fig. S3). Like SST, the large-scale pattern of forced precipitation trends in ALL changes markedly over the course of the historical record, from a predominantly interhemispheric contrast in the early period (Fig. 4a and associated zonal-mean profile) to a more equatorially symmetric structure in the late period (Fig. 4c and associated zonal-mean profile). While there are many regional exceptions to how these large-scale patterns are manifest, the early period has preferentially more drying north of the equator, particularly over Southeast Asia, the Maritime Continent, the western North Pacific, and northern South America, and more wetting south of the equator, especially over the Indian Ocean, central Pacific, and Australia (Fig. 4a), while the late period is dominated by precipitation increases along the equatorial Pacific in addition to the equatorial Atlantic and central Africa, drying over portions of the subtropics, and wetting at middle and high latitudes (Fig. 4c). In relation to the model's climatology, the early period trends represent an eastward extension of

the South Pacific convergence zone (SPCZ), a southward shift of the Indian Ocean convergence zone (IOCZ), and a weakening of the rainfall maximum over the western tropical Pacific (Fig. 4a). In contrast, the late period trends represent an equatorward intensification of the Pacific (and Atlantic) ITCZ, a retraction of the SPCZ, and a weakening of the IOCZ (Fig. 4c). Precipitation trends in the middle period resemble those in the early period but with reduced amplitude over the Pacific sector (Fig. 4b). Regional exceptions to the large-scale patterns described above include drying trends over South Africa in the early and middle periods and wetting trends over the northwestern Indian Ocean in all three periods. The Southern Ocean shows positive precipitation trends in all three periods, which amplify and expand with time.

Like SST, the resemblance between the large-scale patterns of precipitation trends in AER (Figs. 4d,e) and ALL (Figs. 4a–c) is highest in the early period [r(ALL, AER) = 0.72 global, 0.84 tropics] and gradually diminishes over time [middle period r(ALL, AER) = 0.56 global, 0.55 tropics; late period r(ALL, AER) = 0.23 global, 0.21 tropics]. This behavior is also evident in the zonal-mean trend profiles. In the early period, the spatial trend amplitudes are generally larger in AER compared to ALL (Figs. 4d,a). In the middle period, the AER-induced drying over the equatorial Pacific and weak wetting within the ITCZ to the north are in

striking contrast to the features in ALL, as are the opposite-signed trends over the Southern Ocean (cf. Figs. 4e,b). Although the pattern correlation is low in the late period, AER and ALL share certain regional features, for example wetting over eastern North America, Europe, and Africa, and drying over Southeast Asia (Figs. 4f,c).

It is interesting to note the differences in AER-induced precipitation trends over the tropical Pacific between the early and middle periods (Figs. 4d,e). In particular, there is a large degree of equatorial symmetry within the tropical Pacific in the middle period, with drying along the equator and wetting within the ITCZ and SPCZ, in contrast to the antisymmetric pattern that prevails in the early period. A similar structural change is also apparent in the SST trends (Figs. 3d,e). We speculate that this structural change results from the altered distribution of regional AOD trends in the AER simulations, in particular the fact that AOD trends in the middle period are predominantly located in the tropics, whereas those in the early period also include a NH midlatitude component which would drive an interhemispheric shift (recall Figs. 2a,b). The negative AOD trends over Europe and eastern North America in the late period are likely responsible for inducing positive precipitation trends north of the equator in the tropical Atlantic and Africa, as well as local precipitation increases over Europe and eastern North America (Fig. 4f).

Like SST, the patterns of GHG-induced precipitation trends are similar in all three periods, with generally increasing amplitudes over time (Figs. 4g–i and accompanying zonal-mean profiles). GHGs produce an increase in precipitation along the equator in the Pacific and Atlantic, with compensating drying directly to the north and south. In addition, wetting occurs in the extratropics of both hemispheres and over the northern Indian Ocean and Southeast Asia, while bands of drying occur over the equatorial Indian Ocean and the subtropical North Atlantic. These signals become more statistically significant over time as their amplitudes increase. Consistent with SST, the pattern correlations between precipitation trends in ALL and GHG strengthen over time, with low values in the early period (0.16 global, 0.15 tropics), increasing slightly in the middle period (0.28 global, 0.24 tropics) and attaining maximum values in the late period (0.78 global, 0.79 tropics). This behavior is also seen for the zonal-mean trend profiles.

Finally, it is interesting to note the structural similarity (but opposing sign) of the AER and GHG induced precipitation trends during the middle period, especially in the tropics [r(AER, GHG) = −0.40; Figs. 4e,h]. This is also apparent for the accompanying SST trends, not just in the tropics but also in the extratropics [r(AER, GHG) = −0.62; Figs. 3e,h]. The structural similarity between AER and GHG in the middle period is also clear from the zonal-mean profiles for both SST (Fig. 3) and precipitation (Fig. 4). We speculate that the common structure during the middle period results from the predominance of tropical AER forcing, which may mimic the way well-mixed GHGs affect the climate system (albeit with opposite sign).

d. Evolving pattern correlations of forced trends: 1930–2080

Here, we provide a more systematic evaluation of the evolving contributions of AER and GHG to large-scale patterns of forced trends in ALL by calculating r(AER, ALL) and r(GHG, ALL) for running 50-yr trends during 1930–2080 (note the extension beyond the historical period for this analysis). The pattern correlations are computed for both global and tropical domains. Results for precipitation are insensitive to the domain chosen, since precipitation trend amplitudes are much larger in the tropics than the extratropics; hence, we report only the tropical values. For precipitation, r(ALL, AER) is highest (>0.8) for trends beginning in the 1930s, dropping rapidly to between 0.2 and 0.3 for trends starting in the 1960s–90s, followed by a slight rise to around 0.5 for trends beginning after 2010 (Fig. 5a). The increase at the end of the record is associated with a projected reversal of AER-induced AOD trends over Southeast Asia in the RCP8.5 scenario (Fig. S4). The opposite behavior is seen for r(ALL, GHG), with minimum values (<0.3) for trends beginning before 1950, rising rapidly to a maximum of about 0.9 for trends starting in the mid-1980s and thereafter (Fig. 5a). The two pattern correlation curves cross in 1954 (i.e., the 1954–2003 trend period) at a value of 0.42. This 50-yr period, centered in the late 1970s, marks the transition between an aerosol-dominated pattern of forced trends in ALL to a GHG-dominated one. Similar results are found for SST in terms of r(AER, ALL) and r(GHG, ALL), with nearly identical timing and comparable magnitude of the crossover point (Figs. 5b,c). Compared to precipitation and tropical SST, global SST shows a more abrupt rise of r(AER, ALL) around 1980 to peak values of about 0.8 thereafter (Fig. 5c). This sharp transition is coincident with the onset and projected continuation of declining AOD over North America and Eurasia, and is manifest as a reversal in the sign of SST anomalies in both the North Pacific and North Atlantic (not shown).

It is also interesting to compare the evolving pattern correlations between AER and GHG (Figs. 5d–f). Both precipitation and SST show sizeable negative r(AER, GHG) for trends beginning in the late 1940s to mid-1950s
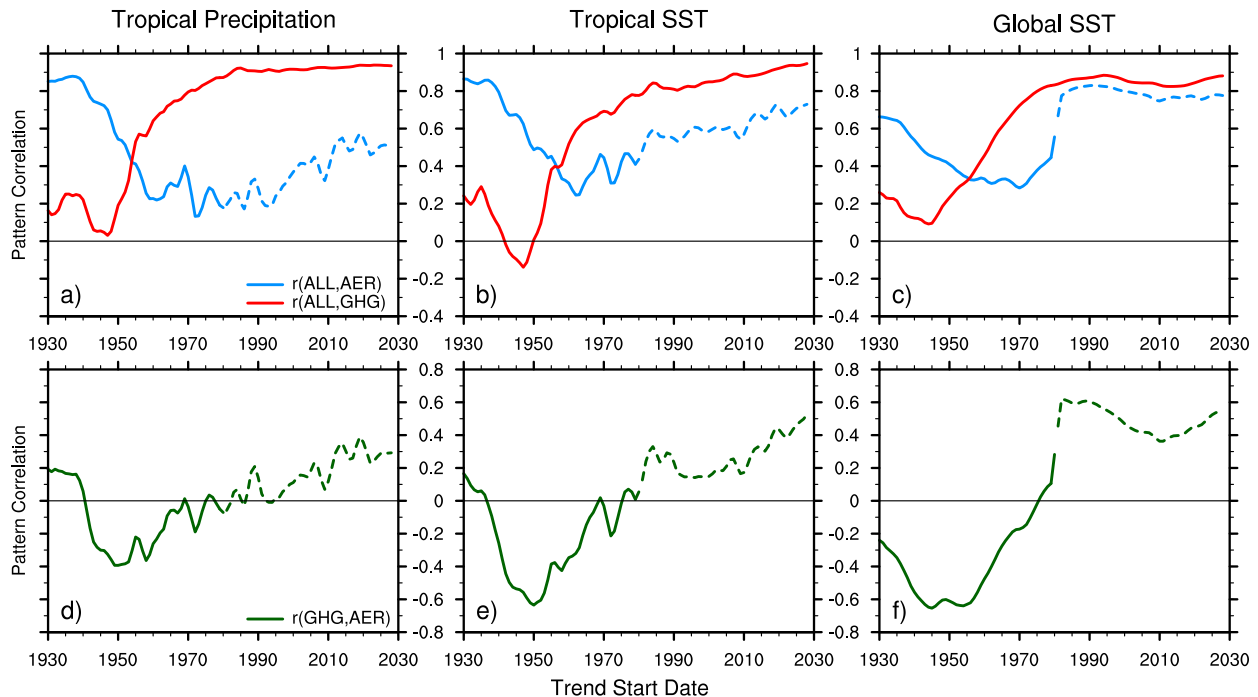
FIG. 5. Pattern correlations between ensemble-mean running 50-yr trends in ALL and AER [r(ALL, AER); blue curves] and between ALL and GHG [r(ALL, GHG); red curves] for (a) tropical precipitation, (b) tropical SST, and (c) global SST. Pattern correlations between ensemble-mean running 50-yr trends in GHG and AER [r(GHG, AER); green curves] for (d) tropical precipitation, (e) tropical SST, and (f) global SST. The time axis denotes the start year of each 50-yr trend. Note that (a)–(c) share the same y-axis labels, and (d)–(f) share the same y-axis labels. All pattern correlation curves have been smoothed with a three-point average for clarity. Dashed curves are based on industrial AER only. Results for global precipitation are nearly identical to those for tropical precipitation.

(minimum values of -0.41 for precipitation; -0.63 and -0.65 for tropical and global SST, respectively), consistent with the middle period trend maps shown in Figs. 3 and 4. As discussed earlier, these anticorrelations may be related to a geographical shift in aerosol emissions, in particular strong tropical AOD increases in the absence of extratropical AOD changes (recall Fig. 2e). It is noteworthy that the strongest anticorrelations occur at about the same time as the transition between an aerosol-dominated pattern of forced trends in ALL to a GHG-dominated one, which has implications for the amplitude of forced trends in ALL (see section 3e). Global SST also shows a sharp transition to positive r(AER, GHG) values (0.4–0.6) for trends beginning after 1980 (Fig. 5f), coincident with the onset of AOD reductions over the northern continents mentioned above.

e. Evolving magnitudes of forced trend patterns: 1930–2080

Pattern correlations convey the degree of structural similarity between pairs of trend maps, but do not indicate their relative magnitudes. Here we use a spatial "root-mean-square" (rms) measure for quantifying the

amplitude of a trend pattern. To compute the spatial rms, we square the ensemble mean trend values at each grid box, take their spatial average over the domain in question (global or tropical) using area-weighting, and then take the square root. This procedure is repeated for each running 50-yr trend interval. For SST, we first subtract the domain-mean trend from the individual trends at each grid box in order to isolate the spatially varying component (i.e., pattern) of the trends (this step is not needed for precipitation trends, which are dominated by spatial variations). Consistent with the trend maps shown in Figs. 3 and 4, the spatial rms of AER-forced tropical precipitation and SST trends maximize at the beginning of the analysis period (i.e., 50-yr trends starting in the 1930s) whereas those of GHG-induced tropical trends increase steadily with time (Figs. 6a,b). The spatial rms magnitudes of the AER and GHG induced tropical trends are comparable for trend start years ranging from 1955 to 1970 (Figs. 6a,b). The spatial rms characteristics in ALL represent a hybrid between those in AER and GHG, with a relative maximum for tropical trends beginning in the 1930s, a minimum for those beginning in the 1950s, and a monotonic increase thereafter (Figs. 6a,b). The minimum spatial rms in ALL
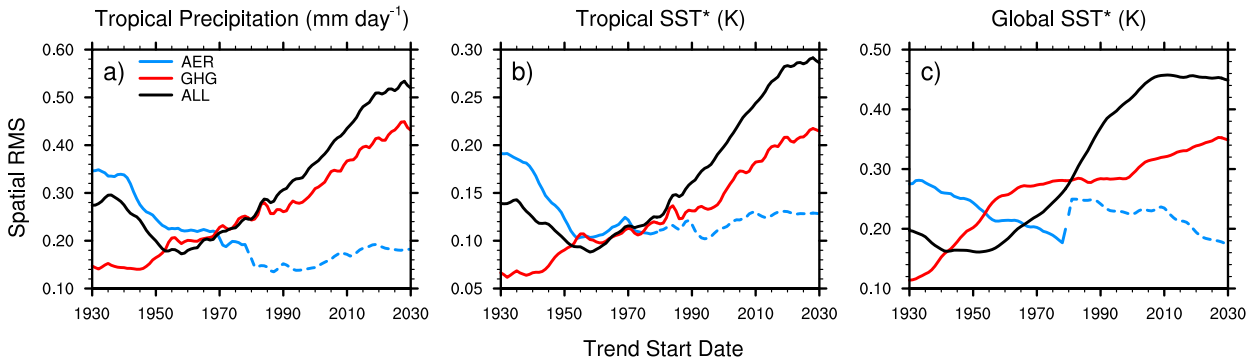
FIG. 6. Spatial RMS of ensemble-mean running 50-yr trends in ALL (black curves), AER (blue curves), and GHG (red curves) for (a) tropical precipitation, (b) tropical SST*, and (c) global SST*, where the asterisk denotes that the domain-mean SST trend has been removed before computing the spatial RMS. The time axis denotes the start year of each 50-yr trend. All curves have been smoothed with a three-point average for clarity. Dashed blue curves are based on industrial AER only. Results for global precipitation are nearly identical to those for tropical precipitation.

results from a combination of reduced AER-driven magnitudes and anticorrelated r(AER, GHG). That is, the minimum amplitude of forced patterns of trends in ALL during the second half of the twentieth century (i.e., 50-yr trends beginning in the 1950s) compared to earlier and later periods is a consequence of reduced aerosol forcing in the NH extratropics combined with similar patterns of response but opposite sign for AER and GHG. The global and tropical SST spatial rms curves are grossly similar, with a more well-defined crossover point (in 1953) between AER and GHG for global SST (Fig. 6c).

f. Additivity of individual forced responses

The comparisons shown above raise the question: To what extent do the forced responses in AER and GHG dominate the forced response in ALL? Recall that ALL includes additional anthropogenic forcings beyond AER and GHG (i.e., stratospheric and tropospheric ozone and land use/land cover changes) as well as natural radiative forcings (i.e., solar and volcanic) and potential nonlinear interactions between the AER and GHG influences. The forced trends in ALL are compared with the sum of the forced trends in AER and GHG (denoted SUM) for each historical period (1930–79, 1950–99, and 1970–2019) in Fig. 7 for SST and Fig. 8 for precipitation (Fig. S5 for precipitation trends as a percentage of the climatology in each period). The large-scale patterns of trends in ALL (panels a–c) and SUM (panels d–f) are very similar, with pattern correlations in excess of 0.9 for all three periods and both variables. Indeed, the differences between ALL and SUM are statistically insignificant over most of the globe (differences shown in panels g–i of Figs. 7 and 8), with some regional exceptions as follows. SST trends in the

early period show significantly larger cooling over the western North Pacific and subpolar North Atlantic (Fig. 7g) while those in the late period show significantly stronger warming over the sub-Arctic North Pacific and Atlantic (Fig. 7i) in SUM compared to ALL. Portions of the Southern Ocean also show significant differences in SST trends in the middle and late periods, in addition to the Gulf Stream Extension in the middle period (Fig. 7h). Precipitation trends over the central tropical Pacific in the early period and the northeastern North Atlantic in the middle period are significantly greater in SUM compared to ALL (Figs. 8g,h, and accompanying zonal means), whereas those over the Southern Ocean in the late period are significantly weaker (Fig. 8i and accompanying zonal means). The physical origins of these statistically significant regional differences merit further investigation, including the roles of natural radiative forcings (Stevenson et al. 2019), southern polar stratospheric ozone changes (Solomon et al. 2015), and nonlinear interactions between AER- and GHG-induced changes in ocean circulation, sea ice, and terrestrial snow cover (Deng et al. 2020; Zhao et al. 2019). Over most of the globe, however, the combined effects of AER and GHG dominate the forced trends in temperature and precipitation in ALL during the historical period.

g. How detectable is the forced trend in a single realization?

Up to now, we have focused on the evolution of forced (i.e., ensemble mean) trends in the ALL, AER, and GHG LEs. How detectable are these forced responses in any single ensemble member? The answer to this question has direct implications for the attribution trends in the observational record (see section 3h). To illustrate the diversity of 50-yr trends across individual
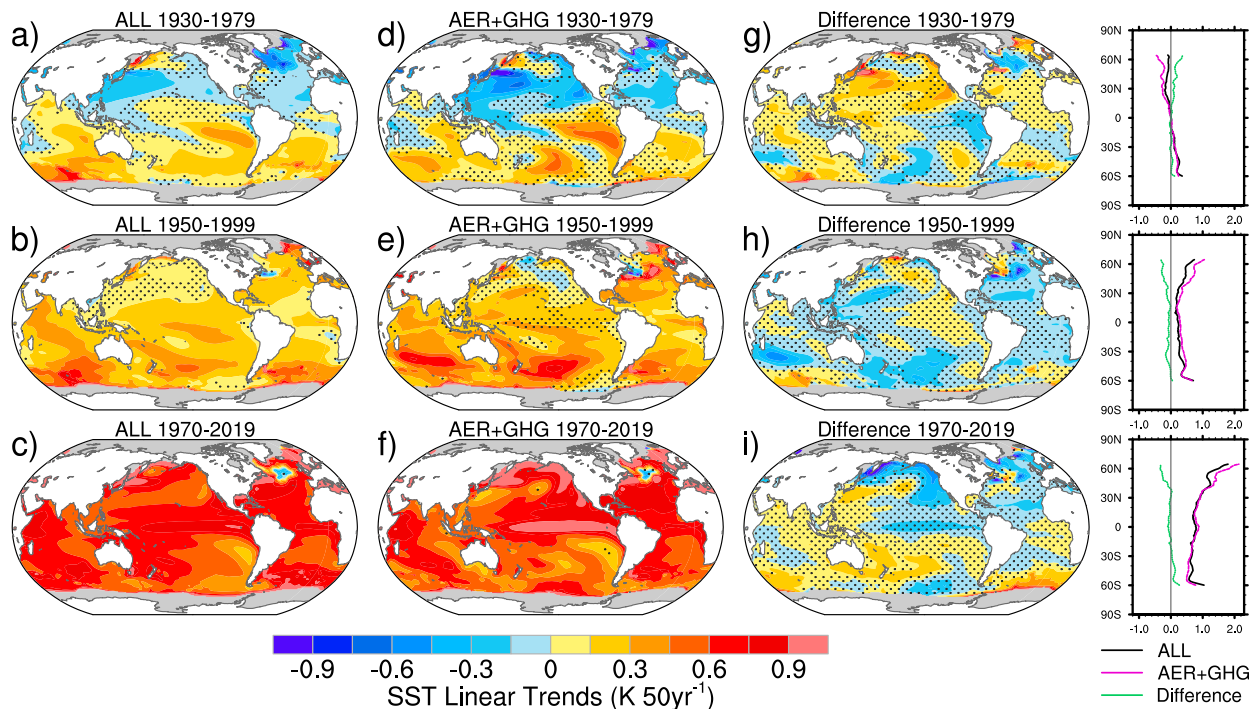
FIG. 7. Linear trends in CESM1 ensemble-mean SST [K (50 yr)$^{-1}$] based on (a) ALL 1930–79; (b) ALL 1950–99; (c) ALL 1970–2019; (d) AER + GHG 1930–79; (e) AER + GHG 1950–99; (f) AER + GHG 1970–2019; (g) ALL minus AER + GHG 1930–79; (h) ALL minus AER + GHG 1950–99; and (i) ALL minus AER + GHG 1970–2019. Stippled regions indicate insignificant values at the 90% confidence level based on a two-sided t test. Gray shading at the poles denotes regions with sea ice. Panels on the right show zonal-mean profiles (60°S–65°N) of the trend maps in each row: ALL (black), AER + GHG (purple), and their difference (green).

members of a given LE (see also Deser et al. 2016), we select two members of ALL with contrasting trends in the early period (Figs. 9a–f) and two members with contrasting trends in the late period (Figs. 9g–l). In the early period, member A shows positive precipitation trends in the eastern tropical Pacific and negative trends in the west (Fig. 9e), similar to the pattern of the forced trend but with much larger amplitude (Fig. 9d). In contrast, member B shows a pronounced drying trend across the entire equatorial Pacific, accompanied by weaker wetting trends to the north and south, a pattern that bears almost no resemblance to the forced trend (Fig. 9f). The associated tropical Pacific SST trends also show distinctive patterns that are physically consistent with the precipitation trends: member A shows warming in the east and cooling in the west, while member B shows cooling that extends across most of the equatorial Pacific (Fig. 9b). The late period shows a similar diversity as the early period, despite the larger global warming signal (Figs. 9h,i,k,l). Indeed, precipitation trends in members A and B during 1970–2019 are of opposite sign over the tropical Pacific, consistent with their contrasting trends in zonal SST gradient. The fact that 50-yr trends in individual ensemble members can be so

different, and can contrast so markedly from the forced trends, attests to the large contribution from internal variability. Such internal variability must be taken into account when interpreting transient and inferred equilibrium climate sensitivity estimates based on observations during the last 50 years, particularly in light of recent work that highlights the sensitivity of these quantities to patterns of SST trends in the tropical Indo-Pacific as a result of their outsized effects on global-scale radiative feedbacks (Jiménez-de-la-Cuesta and Mauritsen 2019; Dong et al. 2019).

We now generalize these anecdotal results on the relative contributions of internal variability and external forcing in individual realizations to the full set of ensemble members and all 50-yr running trend periods during 1930–2080. We use pattern correlations as a metric to summarize the degree of structural resemblance between each individual member's trend and the ensemble-mean trend. For the ALL ensemble, this pattern correlation is denoted $r(\text{ALL}_i, \text{ALL}_{em})$, where i is the trend in ensemble member i and em is the ensemble mean trend. Similar definitions are used for the AER and GHG ensembles [i.e., $r(\text{AER}_i, \text{AER}_{em})$ and $r(\text{GHG}_i, \text{GHG}_{em})$]. We also assess the likelihood that an

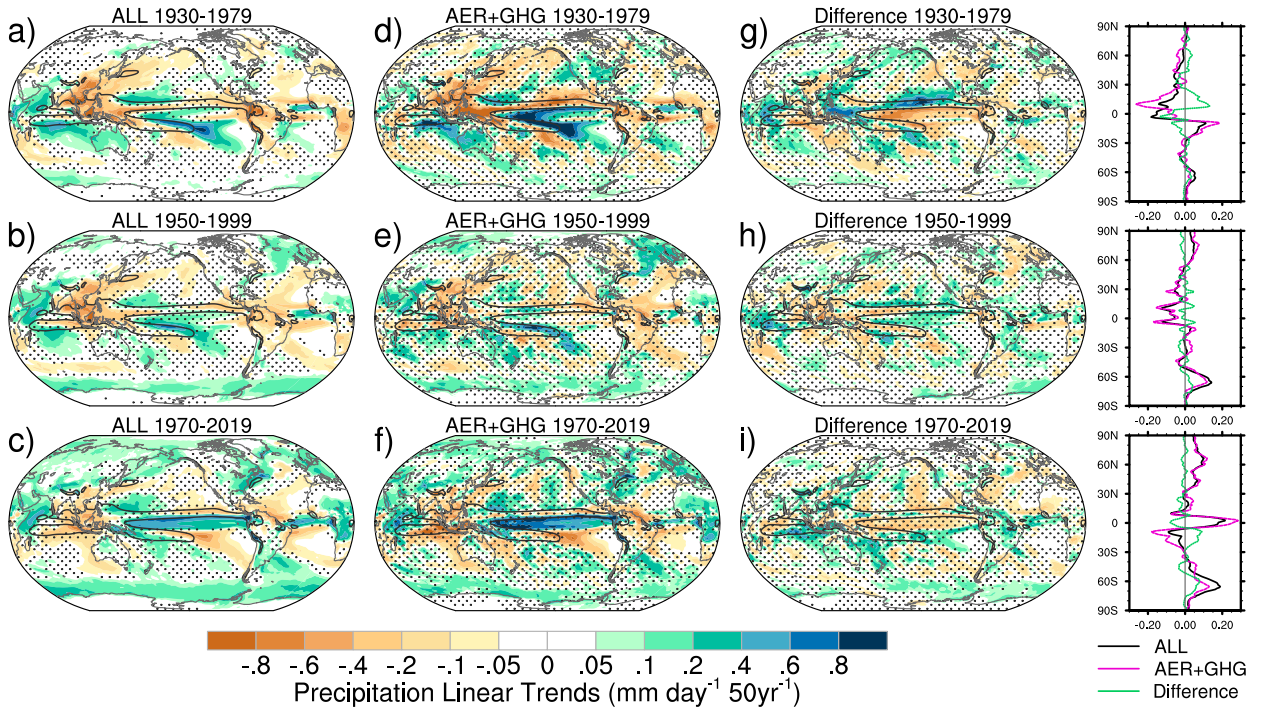FIG. 8. As in Fig. 7, but for precipitation [mm day^{-1} (50 yr)$^{-1}$]. The contours show the 6 mm day^{-1} isopleth of the precipitation climatology (1930–2019) from ALL. Panels on the right show zonal-mean profiles of the trend maps in each row: ALL (black), AER + GHG (purple), and their difference (green).

individual member's trend pattern could have occurred in the absence of external forcing by making use of the 1800-yr CESM1 preindustrial control simulation (Kay et al. 2015). Specifically, we compute trends for 72 overlapping 50-yr segments of the control simulation (i.e., years 401–450, 426–475, 451–501, etc.), and then compute pattern correlations between each of these control trends and the trends in ALL$_{em}$, AER$_{em}$, and GHG$_{em}$. If less than 5% of these control pattern correlations exceeds the value of r(ALL$_i$, ALL$_{em}$), then the trend in member i of the ALL ensemble is unlikely to have occurred without external forcing. Similar logic is applied to the AER and GHG ensembles.

Individual members of ALL show a wide range of pattern correlations with the forced response, especially for trends starting before 2000 (Figs. 10a,d,g). For example, r(ALL$_i$, ALL$_{em}$) for precipitation and tropical SST ranges from about 0.2 to 0.85 for trends beginning in the 1930s and from about 0.1 to 0.7 for trends beginning in the 1950s–early 1960s (Figs. 10a,d), with a slightly narrower spread (approximately 0.3–0.8) for global SST during these periods (Fig. 10g). These ranges narrow considerably for future trends beginning after 2010, to about 0.6–0.9 for precipitation and tropical SST, and about 0.8–0.95 for global SST. The pattern correlations r(ALL$_i$, ALL$_{em}$) are unlikely to have occurred by

chance without external forcing, except for precipitation trends beginning between 1940–74, tropical SST trends beginning in the 1930s and 1950s–60s, and global SST trends beginning in the late 1950s (with some intermittent exceptions; maroon bars along the bottom of Figs. 10a,d,g).

The average r(ALL$_i$, ALL$_{em}$) across the individual ensemble members indicates the degree to which the forced trend pattern is detectable in a single realization, on average. For precipitation and tropical SST, the average r(ALL$_i$, ALL$_{em}$) is about 0.60–0.65 for trends starting in the 1930s, falling to about 0.45 for trends starting in the mid-1950s; the "1930s" value is not reached again until trend start years in the early 1990s, and rises thereafter to a maximum value of 0.80–0.85 for trends starting after 2015 (thick black curves in Figs. 10a and 10d). The average r(ALL$_i$, ALL$_{em}$) is slightly higher for global SST than the other variables, with values around 0.6 for trends starting before about 1960 and increasing to 0.9 for trends beginning after 2000 (thick black curve in Fig. 10g). The temporal character of the average r(ALL$_i$, ALL$_{em}$) curves is consistent with the changing amplitudes of the forced trend patterns (recall Fig. 6).

Another useful metric of detectability of forced trend patterns in individual realizations is the percentage of
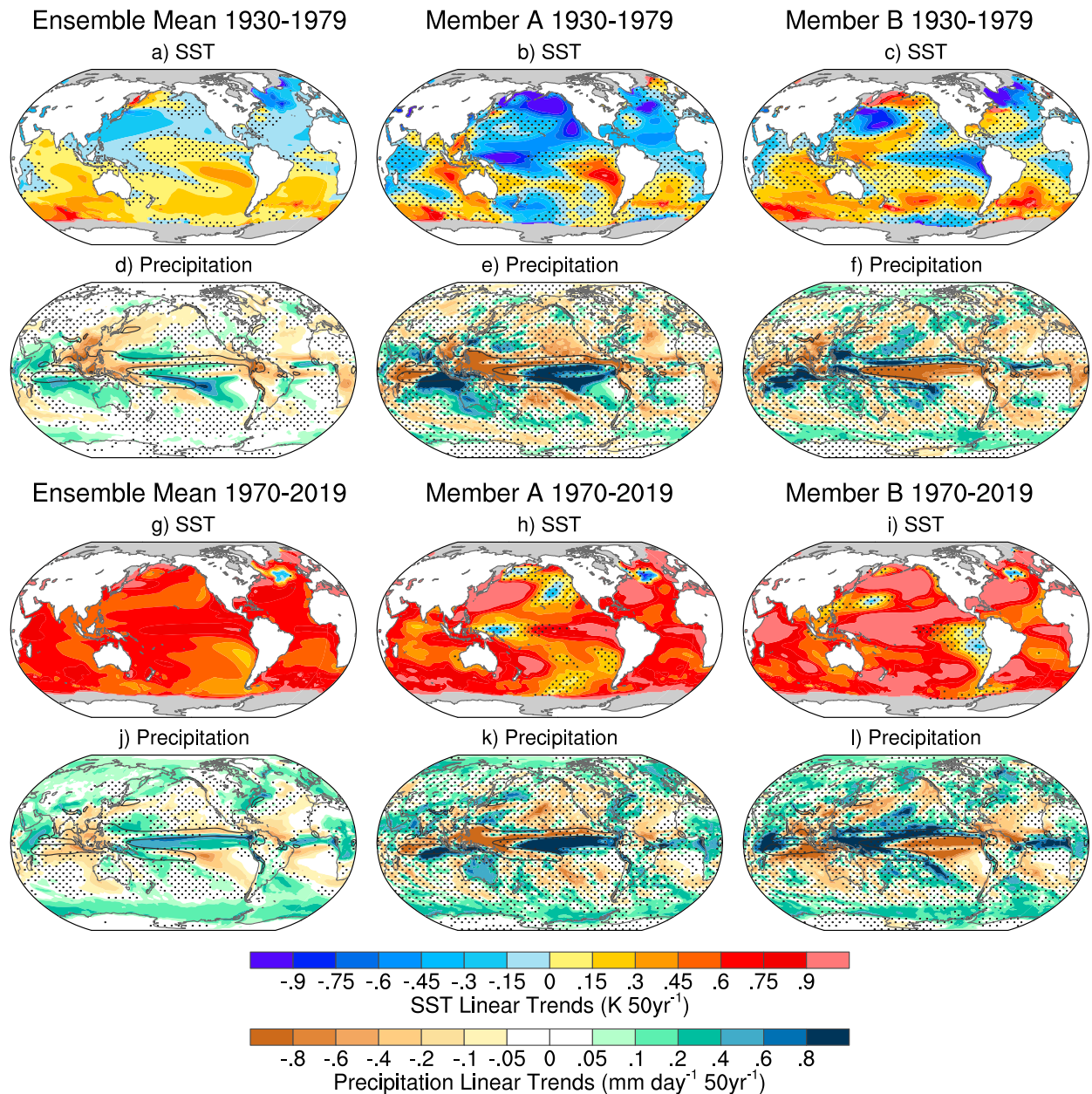
FIG. 9. Linear trends from CESM1 ALL for (a) ensemble-mean SST 1930–79; (b) member A SST 1930–79; (c) member B SST 1930–79; (d) ensemble-mean precipitation 1930–79; (e) member A precipitation 1930–79; (f) member B precipitation 1930–79; (g) ensemble-mean SST 1970–2019; (h) member A SST 1970–2019; (i) member B SST 1970–2019; (j) ensemble-mean precipitation 1970–2019; (k) member A precipitation 1970–2019; and (l) member B precipitation 1970–2019. SST is in units of K $(50 \text{ yr})^{-1}$, and precipitation is in units of mm day^{-1} $(50 \text{ yr})^{-1}$. Stippled regions indicate insignificant values at the 90% confidence level based on a two-sided t test. Gray shading at the poles in SST panels denotes regions with sea ice. The contours on the precipitation panels show the 6 mm day^{-1} isopleth of the precipitation climatology (1930–2019) from ALL.

ensemble members with $r(\text{ALL}_i, \text{ALL}_{em}) > 0.71$ (>0.86), corresponding to $>50\%$ ($>75\%$) of shared spatial variance with the forced response. This metric is displayed by the horizontal colored bars centered at the two pattern correlation thresholds in Fig. 10. For precipitation, $<10\%$ of members exceed the 50% threshold for trends

beginning earlier than the mid-1990s, while $>70\%$ of the members do so for trends beginning after the early 2010s; less than 10% of members exceed the 75% threshold for all trends regardless of start year (Fig. 10a). Similar percentages are found for tropical SST (Fig. 10d). For global SST, more than 90% of members exceed the
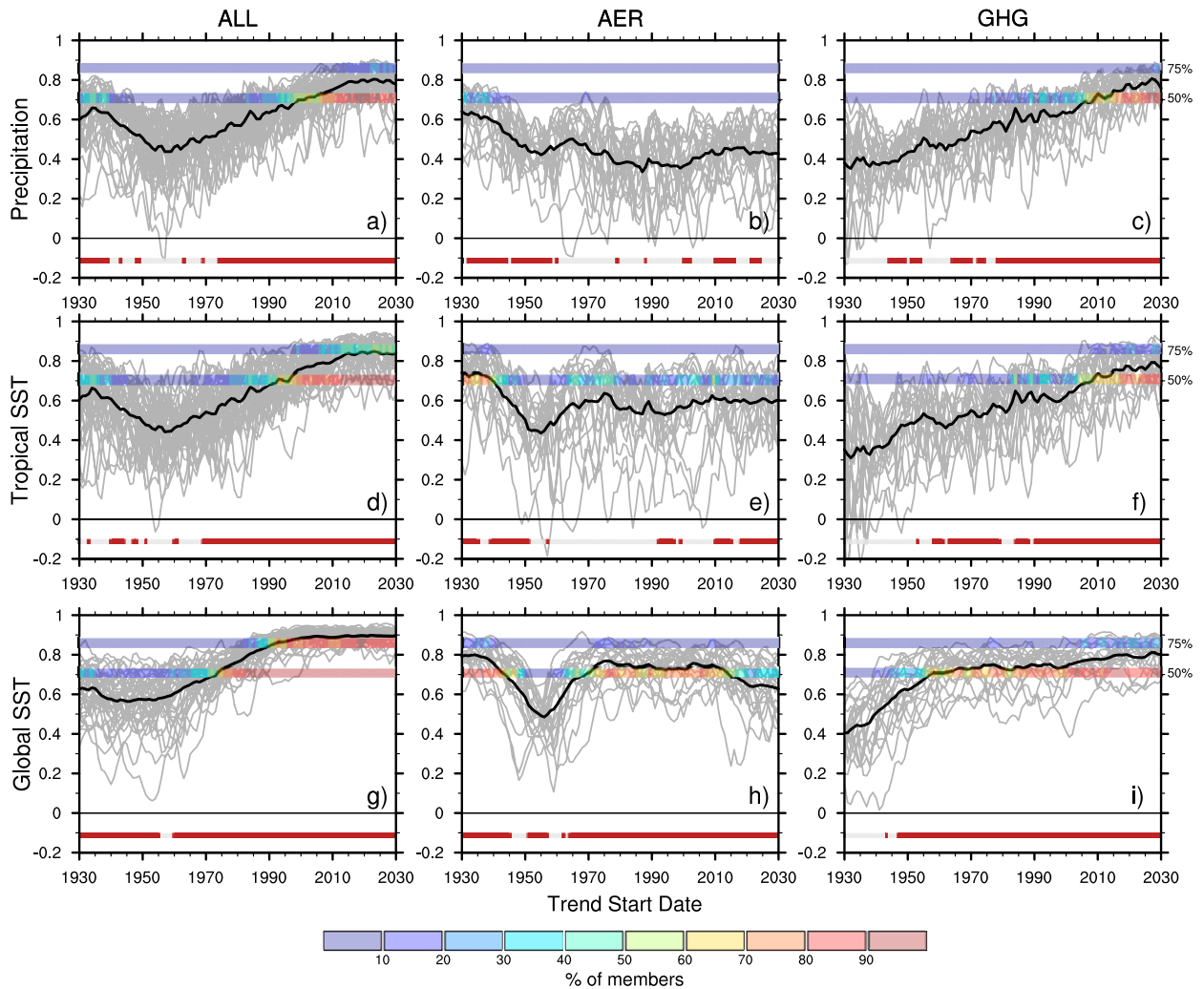
FIG. 10. Pattern correlations (gray curves) of running 50-yr trends between each individual ensemble member and the ensemble mean of (a) ALL tropical precipitation; (b) AER tropical precipitation; (c) GHG tropical precipitation; (d) ALL tropical SST; (e) AER tropical SST; (f) GHG tropical SST; (g) ALL global SST; (h) AER global SST; and (i) GHG global SST. Thick black curves are the average of the gray curves. Lower and upper horizontal colored bars across the top of each panel show the percentage of ensemble members with a pattern correlation exceeding 0.71 and 0.86, corresponding to 50% and 75% variance explained, respectively. Maroon line segments at the bottom of each panel indicate the trend intervals that are significant with respect to the control simulation (see text for details). The time axis denotes the start year of each 50-yr trend. Results for global precipitation are nearly identical to those for tropical precipitation.

50% variance threshold for trends beginning after the mid-1970s, and about 50% of members exceed the 75% threshold for trends starting after 2000 (Fig. 10g). These results are a sobering reminder that the chances of obtaining a trend pattern that closely resembles the forced trend pattern in a single ensemble member are low for any 50-yr interval during the historical period, with clear implications for interpreting the observational record (model biases aside).

The AER (Figs. 10b,e,h) and GHG (Figs. 10c,f,i) ensembles also show a large range of pattern correlations with the forced response across individual members,

typically about 0.4 units for precipitation and tropical SST, and 0.3 units for global SST. Like ALL, the average $r(AER_i, AER_{em})$ and $r(GHG_i, GHG_{em})$ evolve in concert with the amplitude of the forced trend patterns, decreasing over time for AER (from about 0.6–0.8 for trends starting in the 1930s to about 0.4–0.6 for trends starting in the 2030s: thick curves in Figs. 10b,e,h) and increasing over time for GHG (from about 0.3–0.4 for trends starting in the 1930s to about 0.8 for trends starting in the 2030s: thick curves in Figs. 10c,f,i). There is also a conspicuous minimum in average $r(AER_i, AER_{em})$ for tropical and global SST trends starting in

the 1950s (values around 0.45–0.50; Figs. 10e,h). In both the AER and GHG ensembles, <10% of members exceed the 75% variance threshold throughout the analysis period for all three quantities (upper horizontal bar in Figs. 10b,c,e,f,h,i). The 50% variance threshold is exceeded by 70%–80% of AER members for global SST trends starting in the 1930s, and by 70%–80% of GHG members for trends in all three quantities starting later than the mid-2010s (lower horizontal bar in Figs. 10b,c,e,f,h,i). These results indicate that even for the AER and GHG ensembles, the chances of obtaining a trend pattern that closely resembles the forced trend pattern in a single ensemble member are low, except at the very end of the record for GHG and the very beginning of the record for AER global SST. A complementary analysis of the ensemble spread in the amplitude of large-scale trend patterns is given in Fig. S6.

h. Interpretation of observed trends in the context of CESM1

The model results shown above have implications for the interpretation of trends in observations, model biases notwithstanding. In particular, if the model's signal-to-noise ratio is realistic, then the prominence of internal variability relative to the forced response in any single ensemble member suggests that it is challenging to extract the forced response in observed patterns of 50-yr SST and precipitation trends (see also Deser et al. 2016). In addition, analysis of observations is hampered by issues of data quality, homogeneity, and spatial and temporal coverage. Although it is beyond the scope of this study to conduct a formal "detection and attribution" analysis (e.g., Santer et al. 2019; Bonfils et al. 2020), we examine the observed evolution of 50-yr SST and precipitation trend patterns within the context of the CESM1 ALL, AER, and GHG LEs whose sizes allow for the first time a quantitative assessment of AER and GHG effects on regional scales during 1930–2018.

Maps of observed SST and precipitation trends for the three overlapping 50-yr periods are shown in Fig. 11, along with ensemble-mean trends from ALL (ALL_{em}) for direct comparison. On a global scale, observed SST trends show an acceleration of warming over the historical period (Figs. 11a–c), consistent with the forced signal in ALL (Figs. 11c–f; see also Fig. 1a for GMST). The spatial patterns of observed SST trends, as expected from the internal variability inherent in the single observed realization, show similarities and differences with the forced trends in ALL. In the early period and similar to ALL, observed SSTs cool over most of the North Atlantic and eastern North Pacific, and warm over much of the Indian Ocean, South Atlantic, and South Pacific, although their amplitudes are considerably larger than

those of the model's forced response (Figs. 11a,d). Other areas show opposite sign trends between observations and ALL_{em} in the early period, such as the western half of the North Pacific and the southeastern tropical Pacific and Atlantic. Note that data coverage over the Southern Ocean and southeast tropical Pacific is very limited (Fig. S7), so that uncertainty in SST trends in these regions is higher than elsewhere. The pattern correlation between SST trends in observations and ALL_{em} [r(OBS, ALL_{em})] for the early period is 0.03 for the tropics and 0.39 for the global domain. The large-scale structure of observed SST trends evolves in the middle period, with an amplification of warming over the Indian Ocean and eastern tropical Pacific and Atlantic, a reduction in cooling over the North Atlantic and an opposite-signed pattern over the North Pacific compared to the early period (Fig. 11b). The observed trend magnitudes in the middle period are considerably larger than those in ALL_{em} (Fig. 11e), and the pattern correlation with ALL_{em} is modest (0.23 for the tropics and 0.25 for the global domain). The observed warming pattern continues to evolve in the late period, with relative maxima near the equator in all three ocean basins as well as the subpolar North Pacific and most of the North Atlantic, and relative minima south of Iceland, the tropical South Atlantic and southeast Pacific, and the Southern Ocean, which exhibit cooling (Fig. 11c). Some of these features are evident in ALL_{em} (Fig. 11f), but the pattern correlations remain modest (0.28 for the tropics and $r = 0.31$ for the global domain).

A comparison of precipitation trends in observations (GPCC) and ALL_{em} is limited to land areas before the satellite era (Figs. 11g–i). Overall, the resemblance of large-scale spatial patterns of terrestrial precipitation trends between observations and ALL_{em} is low, as evidenced by the weak pattern correlations: 0.16 for 1930–79, 0.07 for 1950–99, and 0.04 for 1970–2018 in the tropics, with similar values for the global domain. In the early period (Figs. 11g,j), similarities between GPCC and ALL_{em} include drying of the Sahel, the Caribbean, and the Maritime Continent, and wetting over Australia, northeast Brazil, and parts of the United States and eastern Eurasia (although GPCC shows generally larger amplitudes than ALL_{em}). In addition, the pronounced early-period drying over Southeast Asia in ALL_{em} is confined to coastal locations in GPCC, and early-period trends over South Africa and Argentina are opposite in GPCC and ALL_{em}. Precipitation trends in the middle period (Figs. 11h,k) are similar to those in the early period, except for the increased wetting over northern Europe and the reversal to drying over the Mediterranean in both GPCC and ALL_{em}; there is also increased drying over the Sahel and South Africa in GPCC, opposite to that in
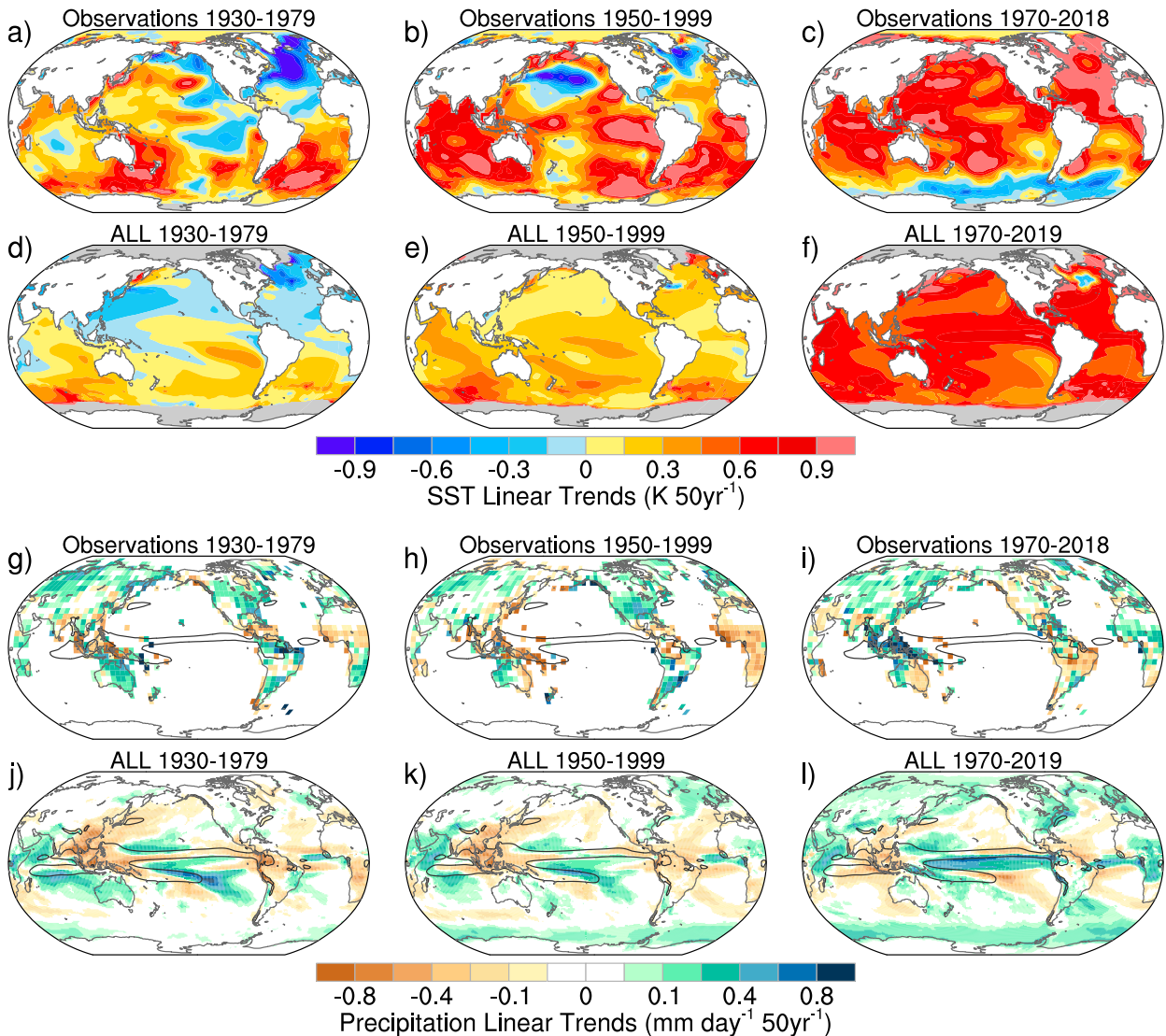
FIG. 11. Linear SST trends [K (50 yr)$^{-1}$] for (a) observations 1930–79; (b) observations 1950–99; (c) observations 1970–2018; (d) ALL ensemble-mean 1930–79; (e) ALL ensemble-mean 1950–99; and (f) ALL ensemble-mean 1970–2019. Also shown are linear precipitation trends [mm day^{-1} (50 yr)$^{-1}$] for (g) observations 1930–79; (h) observations 1950–99; (i) observations 1970–2018; (j) ALL ensemble-mean 1930–79; (k) ALL ensemble-mean 1950–99; and (l) ALL ensemble-mean 1970–2019. Gray shading at the poles in SST panels denotes regions with sea ice. The contours on the precipitation panels show the 6 mm day^{-1} isopleth of the precipitation climatology. ERSSTv5 and GPCC are used for observations of SST and precipitation, respectively. White regions over the oceans in the observed precipitation panels indicate missing data.

ALL$_{em}$. In the late period (Fig. 11i), observed trends over the Maritime Continent, eastern Australia, Brazil, and the Sahel have reversed sign from the earlier periods; of these, only the wetting trend over the Sahel is consistent with the sign of the trends in ALL$_{em}$ (Fig. 11l).

Without better spatial coverage over the oceans, it is difficult to make any statements about observed precipitation trends in marine areas including the tropical convergence zones. However, precipitation trends during 1979–2018 from GPCP, which provides near-global

coverage by incorporating satellite data, also show limited spatial correspondence with ALL$_{em}$ (pattern correlation = 0.17; see maps in Fig. S8).

Last, we provide an integrated perspective on the relative roles of internal variability, GHG, and AER in the evolution of large-scale patterns of 50-yr precipitation and SST trends in observations and ALL. Figures 12a, 12d, and 12g show r(OBS, ALL$_{em}$) for running 50-yr trends during 1930–2018 (blue curves), superimposed upon r(ALL$_i$, ALL$_{em}$) over the extended period 1930–
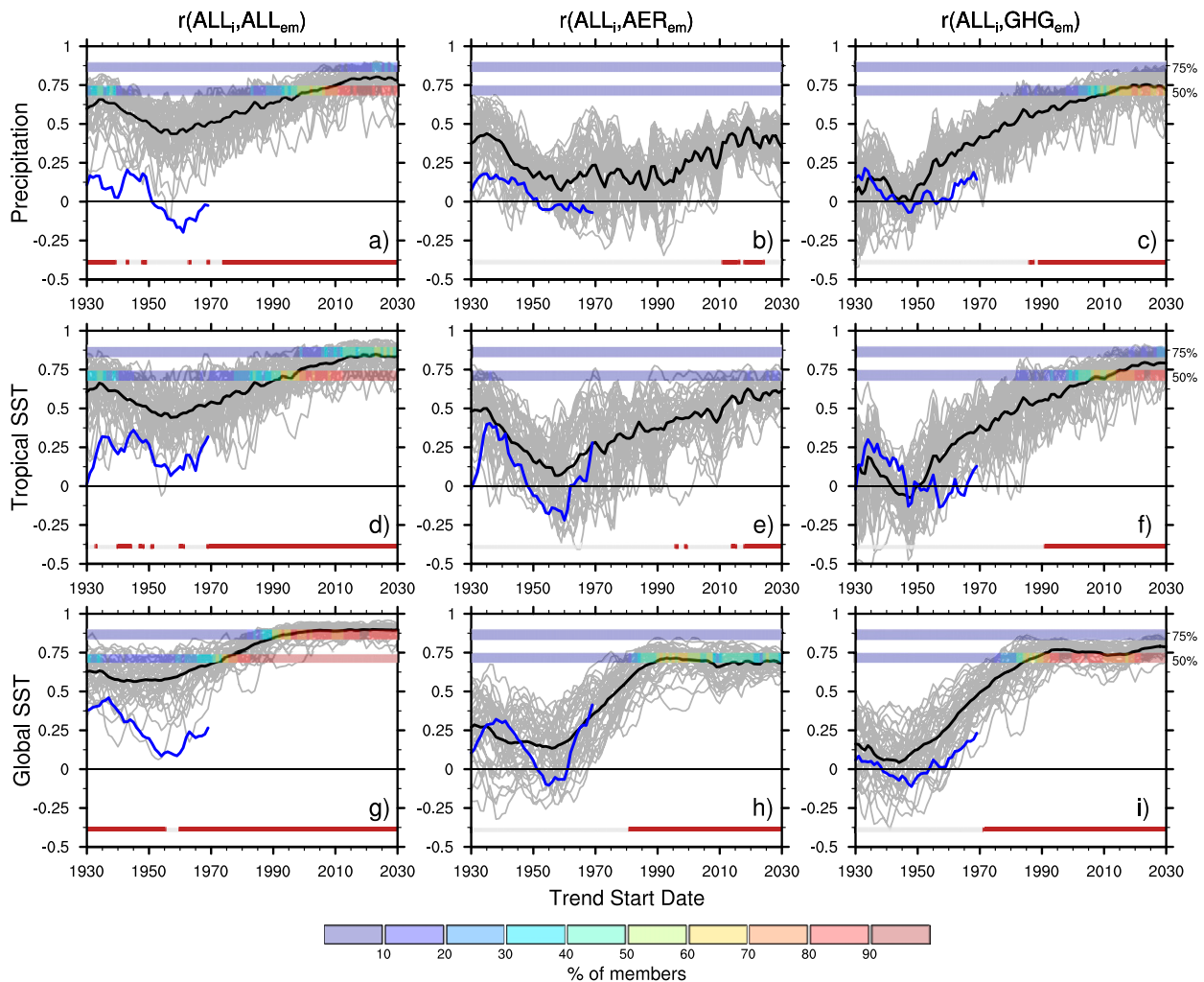
FIG. 12. Pattern correlations (gray curves) of running 50-yr trends between the individual ensemble members (i) of ALL (ALL$_i$) and the ensemble mean (em) of (a) ALL, tropical precipitation; (b) AER, tropical precipitation; (c) GHG, tropical precipitation; (d) ALL, tropical SST; (e) AER, tropical SST; (f) GHG tropical SST; (g) ALL, global SST; (h) AER, global SST; and (i) GHG, global SST. Thick black curves are the average of the gray curves. Lower and upper horizontal colored bars across the top of each panel show the percentage of ensemble members with a pattern correlation exceeding 0.71 and 0.86, corresponding to 50% and 75% variance explained, respectively. Maroon line segments at the bottom of each panel indicate the trend intervals that are significant with respect to the control simulation (see text for details). Blue curves show the pattern correlations between observations and the ensemble means from ALL, AER, and GHG. GPCC and ERSSTv5 are used for observations of precipitation and SST, respectively (results based on HadISST SST are similar; not shown). The time axis denotes the start year of each 50-yr trend. Results for global precipitation are nearly identical to those for tropical precipitation.

2080 (repeated from Fig. 10). The r(OBS, ALL$_{em}$) ranks near the bottom or below the ensemble spread of r(ALL$_i$, ALL$_{em}$) regardless of trend start year for precipitation and SST. Masking the simulated precipitation trends according to the evolving spatial coverage in GPCC increases r(ALL$_i$, ALL$_{em}$) by about 0.15, on average, for trends starting before about 1980, widening the gap with r(OBS, ALL$_{em}$) (Fig. 13a). Many factors may play a role in the discrepancy between r(OBS, ALL$_{em}$) and r(ALL$_i$, ALL$_{em}$), including some combination of the following: 1)

uncertainty in anthropogenic aerosol emissions; 2) biases in the model's pattern and/or amplitude of forced response; 3) biases in the model's patterns of internal variability; 4) biases in the model's signal-to-noise of forced response relative to internal variability; 5) a highly unusual occurrence of internal variability in observations; and 6) observational error. Further investigation is needed to address the relative importance of each of these factors; additional discussion is provided in section 5.
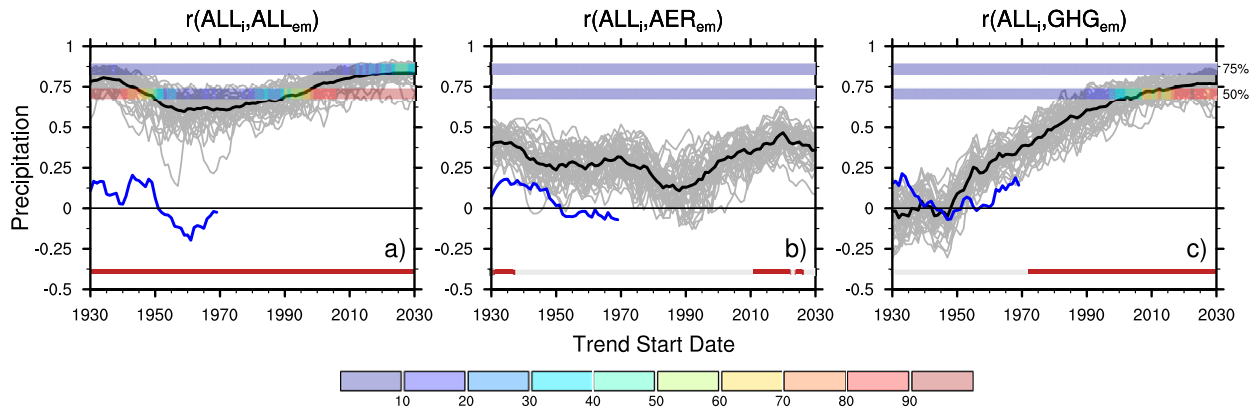
FIG. 13. As in Figs. 12a–c, but for precipitation masked according to the evolving spatial coverage in observations (GPCC).

To determine the individual contributions of AER and GHG to the trend patterns in each member of ALL, we compute $r(\mathrm{ALL}_i, \mathrm{AER}_{\mathrm{em}})$ and $r(\mathrm{ALL}_i, \mathrm{GHG}_{\mathrm{em}})$. The large spread in $r(\mathrm{ALL}_i, \mathrm{AER}_{\mathrm{em}})$ and $r(\mathrm{ALL}_i, \mathrm{GHG}_{\mathrm{em}})$ across the ensemble members indicates substantial uncertainty in the detectability of AER- and GHG-driven trend patterns in any single realization according to our metrics (gray curves in Figs. 12b,c,e,f,h,i). Further, the average $r(\mathrm{ALL}_i, \mathrm{AER}_{\mathrm{em}})$ and average $r(\mathrm{ALL}_i, \mathrm{GHG}_{\mathrm{em}})$ values (thick black curves in Figs. 12b,c,e,f,h,i) fall well below the 50% variance threshold (pattern correlation of 0.71) throughout the historical period. Indeed, this threshold is only met or exceeded for GHG-induced precipitation and tropical SST trends beginning after 2010, and for AER- and GHG-induced global SST trends beginning after 1990. Of these, only the future GHG-induced SST trends exceed the 50% threshold in a majority of ensemble members (colored horizontal bars in Figs. 12f and 12i).

Turning to the observations, we compute $r(\mathrm{OBS}, \mathrm{AER}_{\mathrm{em}})$ and $r(\mathrm{OBS}, \mathrm{GHG}_{\mathrm{em}})$ in analogy with $r(\mathrm{ALL}_i, \mathrm{AER}_{\mathrm{em}})$ and $r(\mathrm{ALL}_i, \mathrm{GHG}_{\mathrm{em}})$ and superimpose the results in Fig. 12 (blue curves). Note that masking the simulated precipitation trends by the evolving spatial coverage in GPCC does not substantially alter the average values of $r(\mathrm{ALL}_i, \mathrm{AER}_{\mathrm{em}})$ and $r(\mathrm{ALL}_i, \mathrm{GHG}_{\mathrm{em}})$, although it narrows their ensemble spread (Figs. 13b,c). $r(\mathrm{OBS}, \mathrm{AER}_{\mathrm{em}})$ mostly falls within the ensemble spread of $r(\mathrm{ALL}_i, \mathrm{AER}_{\mathrm{em}})$, although generally below the average value of $r(\mathrm{ALL}_i, \mathrm{AER}_{\mathrm{em}})$: Figs. 12b,e,h and 13b. Similarly, $r(\mathrm{OBS}, \mathrm{GHG}_{\mathrm{em}})$ lies near the middle of the distribution of $r(\mathrm{ALL}_i, \mathrm{GHG}_{\mathrm{em}})$ for trends starting before about 1950 and within the lower end of the distribution thereafter (Figs. 12c,f,i and 13c). While the observed pattern correlations with the forced trends in AER and GHG are thus generally within the distributions expected from the combined influence of external forcing and internal variability (according to CESM1),

their weak amplitudes (<0.4) indicate that $<20\%$ of the spatial variance in the observed trend patterns is driven by AER or GHG. This estimate pertains only to the pattern correlation metrics used here, and is subject to all of the caveats mentioned above (see further discussion in section 5).

4. Summary

We have studied the evolving roles of anthropogenic aerosols (AER) and greenhouse gases (GHG) in driving large-scale patterns of forced precipitation and SST trends during 1920–2080 using a new set of CESM1 initial-condition large ensembles (LEs). In these new LEs, either industrial aerosols, biomass burning aerosols, or greenhouse gases are kept fixed at early-twentieth-century conditions while all other external anthropogenic and natural forcings vary in time according to historical and future (RCP8.5) scenarios. These new LEs use the same model version and experimental design as the "all forcing" (ALL) CESM1 LE (Kay et al. 2015), allowing a direct assessment of the individual roles of each forcing factor within the context of a background changing climate, obtained by differencing the new LEs from the all-forcing LE. The large number of ensemble members (15–20) in each of the new LEs enables regional impacts of AER and GHG forcing to be isolated from the noise of internal variability. Conversely, the LEs provide a unique perspective on the role of internal variability in limiting detection and attribution of AER and GHG effects in any single realization, and by extension the observational record. Our analysis approach, based on running 50-yr trends, accommodates geographical and temporal changes in both the patterns of forcing and response. The main findings of our study are summarized as follows.

1) Large-scale patterns of forced precipitation and SST trends in ALL evolve over the historical period 1930–2019 from an interhemispheric structure dominated by aerosol effects to a more equatorially symmetric pattern dominated by greenhouse gas influences, with the transition occurring in the late 1970s. The transition phase is characterized by a relative minimum in trend pattern amplitudes in ALL, due to a combination of reduced AER forcing and offsetting effects from AER and GHG. During this phase, AER and GHG drive similar patterns of response, albeit of opposite polarity.

2) Over most of the globe, the sum of the forced trends in AER and GHG is statistically indistinguishable from the forced trends in ALL for both precipitation and SST throughout the historical period. This confirms the dominant roles of AER and GHG externally forced climate change over the historical period. Those areas that do show significant differences are mainly associated with strong ocean currents, deep water formation and sea ice, which could arise from nonlinear interactions between AER and GHG, or from additional (natural and anthropogenic) external influences (e.g., stratospheric ozone depletion, volcanic eruptions, etc.).

3) Internal variability greatly limits the detectability of forced trend patterns in individual realizations of the AER, GHG, and ALL ensembles, especially during the historical period, according to our pattern correlation metric. The average pattern correlation between an individual member's trend and the forced trend in ALL ranges from approximately 0.4 to 0.7 over the course of the historical period, rising to 0.8–0.9 in the future. However, a single member can show pattern correlations as low as 0.2 or as high as 0.8 for the same 50-yr trend interval during the historical period. Qualitatively similar ranges are found for the AER and GHG ensembles. It should also be noted that the forced trend patterns themselves are subject to uncertainty due to the finite number of ensemble members used for estimating them.

4) The model results summarized above highlight a number of challenges for attributing trends in the observational record, an endeavor that is further hampered by data coverage and quality issues as well as model bias. Pattern correlations between observed trends and forced trends in the ALL, AER, and GHG ensembles rank near the bottom of (or in some cases below) the model distributions. This implies likely model biases in one or more of the following: patterns of internal variability; patterns of forced response; and relative magnitudes of forced response and internal variability (i.e., signal-to-noise).

The low (generally <0.4) pattern correlations with observations imply that <20% of the spatial variances of observed SST and precipitation trend patterns are forced, regardless of which 50-yr interval during 1930–2018 is considered, but model biases in addition to uncertainty in the magnitude of anthropogenic aerosol forcing will undoubtedly affect this estimate.

5. Discussion

Our findings are based on a single model with a single scenario of anthropogenic and natural radiative forcings. Structural model uncertainty related to physics and parameterizations as well as uncertainty in radiative forcings, especially those associated with anthropogenic aerosols, remain important caveats to this work. In particular, there is also no consensus to date on how strong aerosol forcing is in the real world (Wilcox et al. 2015), although we note that the magnitude of effective aerosol radiative forcing in CESM1 ($-1.37\,\mathrm{W\,m^{-2}}$: Zelinka et al. 2014) lies within the one-standard-deviation range of plausible estimates (from -1.6 to $-0.6\,\mathrm{W\,m^{-2}}$) according to a recent comprehensive review (Bellouin et al. 2020).

Another important caveat is the degree to which CESM1 realistically simulates both the patterns and magnitudes of internal variability and forced responses, with implications for the signal-to-noise ration and the detectability of forced trends in individual realizations and in the real world. Evaluating internal variability in models is a challenging endeavor, particularly with respect to multidecadal trends given the brevity of the observational record (McKinnon et al. 2017; McKinnon and Deser 2018; Deser et al. 2020). Existing efforts have focused on evaluation of internal variability of trends in terrestrial air temperatures and precipitation (e.g., Thompson et al. 2015; McKinnon and Deser 2018; Beusch et al. 2020. These studies indicate that CESM1 overestimates internal variability of 50-yr trends in terrestrial air temperature at many locations; however, precipitation trend variability shows regions of both underestimation and overestimation. The extent to which these biases in internal trend variability over land extend to marine areas remains to be assessed, along with implications for signal-to-noise and detectability of forced trends.

We have emphasized a large-scale pattern perspective in our analysis, using spatial correlations—over tropical and global domains—as a metric. Our conclusions regarding detectability of forced trends in observations based on this metric may be compromised by model biases in the patterns of internal variability and forced response. Alternate metrics that place less emphasis on regional detail, such as spatially aggregated quantities (Fischer and Knutti 2015), interhemispheric contrasts

(Friedman et al. 2013, 2020), or the use of a limited number of empirical orthogonal functions (EOFs; Bonfils et al. 2020), may result in a higher level of detectability of forced signals in the real world. Conversely, specific regions with greater sensitivity to anthropogenic aerosols, such as the Sahel, Southeast Asia, and Europe, may also have higher and/or more accurate detectability. Finally, application of more sophisticated statistical approaches such as optimal fingerprinting (e.g., Hegerl et al. 1996; Ting et al. 2009), formal detection and attribution (Santer et al. 2019; Bonfils et al. 2020), and novel pattern recognition methods (Barnes et al. 2019; Sippel et al. 2019; Wills et al. 2020) to this new collection of CESM1 LEs may be promising avenues for future work aimed at assessing detectability of trends forced by anthropogenic aerosols and GHGs. Adopting a framework that allows for temporal changes in both the patterns of forcing and of climate response, especially as they relate to regional aerosol emissions, will be important regardless of the approach used. In particular, using a single EOF to capture the evolving impacts of anthropogenic aerosol effects may be inadequate.

The above caveats notwithstanding, our results emphasize the need for caution when using individual realizations from a given model to assess climatic impacts of anthropogenic aerosols and GHGs during the historical period due to confounding effects from internal variability. Combining individual simulations from different models (such as those in the CMIP5 and CMIP6 archives) to reduce internal variability may also be problematic due to the models' diverse representation of aerosol direct and indirect effects (e.g., Bellouin et al. 2020). Further, anthropogenic aerosol precursor emissions differ between CMIP5 and CMIP6, both over the historical period and in future projections, thereby introducing additional uncertainty into their climatic impacts (Samset et al. 2019; Wilcox et al. 2020). These issues emphasize the need for additional "single-forcing" large ensembles with other comprehensive Earth system models to obtain a more robust assessment of the climate impacts of anthropogenic aerosols and associated uncertainties (Bonfils et al. 2020; Swart et al. 2019; Dittus et al. 2020). The ensemble size requirements for such single-forcing LEs remain to be determined and will depend on the particular application and model (Deser et al. 2012; Milinski et al. 2019).

A number of outstanding issues are raised by our findings and remain to be addressed in future work. For example, additional research is needed to understand why the CESM1-simulated patterns of precipitation and SST trends forced by AER and GHG share a common structure during the latter half of the twentieth century (50-yr trends centered in the late 1970s), whereas they are dissimilar in earlier and later periods of the historical record. We hypothesize their common structure may be due to the fact that trends in regional aerosol emissions during the period centered in the late 1970s are located primarily within the tropics, unlike earlier and later periods when there are additional prominent sources and sinks in the northern extratropics, respectively. While additional targeted experiments are needed to test our hypothesis, the results reported by Stuecker et al. (2020) may provide circumstantial evidence for the role of tropical aerosol forcing. In particular, Stuecker et al. (2020) show that when GHG increases are artificially confined to the tropics in CESM1, the structure of the zonal-mean response within the tropics is very similar (albeit of opposite sign) to those of our AER-induced trends during 1950–99 for both SST and precipitation. More generally, additional research is needed to understand the physical mechanisms governing the evolving forced responses to AER and GHG in CESM1, including the potential role of nonlinear interactions between these forcing agents.

Other outstanding issues raised by our findings remain to be addressed in future work. For example, what role do CESM1 biases play in limiting detectability of AER and GHG influences on observed large-scale patterns of precipitation and SST, and what particular aspects of model bias are most important (e.g., patterns versus amplitudes, forced responses versus internal variability, and signal-to-noise ratio)? How much can the signal-to-noise ration of forced climate trends in the CESM1 ALL, AER, and GHG ensembles be enhanced through the application of more advanced statistical approaches, and how does this affect our conclusions regarding detectability of AER and GHG influences on observed large-scale patterns of precipitation and SST trends? Finally, there is scope for repeating our analysis on the all-forcing and single-forcing LEs available from CanESM2 (Bonfils et al. 2020) and CanESM5 (Swart et al. 2019), and from other models as they become available.

Data availability statement. Observational datasets used in this study are available from https://www.esrl.noaa.gov/psd. The CESM1 Large Ensemble simulations used in this study are available from http://www.cesm.ucar.edu/experiments/cesm1.1/LE/#single-forcing and http://www.cesm.ucar.edu/projects/community-projects/LENS.

REFERENCES

Adler, R. F., and Coauthors, 2018: The Global Precipitation Climatology Project (GPCP) monthly analysis (new version 2.3) and a review of 2017 global precipitation. *Atmosphere*, **9**, 138, https://doi.org/10.3390/atmos9040138.

Barnes, E. A., J. W. Hurrell, I. Ebert-Uphoff, C. Anderson, and D. Anderson, 2019: Viewing forced climate patterns through an AI lens. *Geophys. Res. Lett.*, **46**, 13 389– 13 398, https://doi.org/10.1029/2019GL084944.

Bellouin, N., and Coauthors, 2020: Bounding global aerosol radiative forcing of climate change. *Rev. Geophys.*, **58**, e2019RG000660, https://doi.org/10.1029/2019RG000660.

Beusch, L., L. Gudmundsson, and S. I. Seneviratne, 2020: Emulating Earth system model temperatures with MESMER: From global mean temperature trajectories to grid-point-level realizations on land. *Earth Syst. Dyn.*, **11**, 139–159, https://doi.org/10.5194/esd-11-139-2020.

Bonfils, C., B. D. Santer, J. C. Fyfe, K. Marvel, T. J. Phillips, and S. Zimmerman, 2020: Human influence on joint changes in temperature, rainfall and continental aridity. *Nat. Climate Change*, https://doi.org/10.1038/s41558-020-0821-1, in press.

Chung, E., and B. Soden, 2017: Hemispheric climate shifts driven by anthropogenic aerosol–cloud interactions. *Nat. Geosci.*, **10**, 566–571, https://doi.org/10.1038/ngeo2988.

Deng, J., A. Dai, and H. Xu, 2020: Nonlinear climate responses to increasing CO_2 and anthropogenic aerosols simulated by CESM1. *J. Climate*, **33**, 281–301, https://doi.org/10.1175/JCLI-D-19-0195.1.

Deser, C., A. S. Phillips, V. Bourdette, and H. Teng, 2012: Uncertainty in climate change projections: The role of internal variability. *Climate Dyn.*, **38**, 527–546, https://doi.org/10.1007/s00382-010-0977-x.

——, L. Terray, and A. S. Phillips, 2016: Forced and internal components of winter air temperature trends over North America during the past 50 years: Mechanisms and implications. *J. Climate*, **29**, 2237–2258, https://doi.org/10.1175/JCLI-D-15-0304.1.

——, and Coauthors, 2020: Insights from Earth system model initial-condition large ensembles and future prospects. *Nat. Climate Change*, **10**, 277–286, https://doi.org/10.1038/s41558-020-0731-2.

DiNezio, P. N., A. C. Clement, G. A. Vecchi, B. J. Soden, B. P. Kirtman, and S. Lee, 2009: Climate response of the equatorial Pacific to global warming. *J. Climate*, **22**, 4873–4892, https://doi.org/10.1175/2009JCLI2982.1.

Dittus, A. J., E. Hawkins, L. J. Wilcox, R. Sutton, C. J. Smith, M. B. Andrews, and P. M. Forster, 2020: Sensitivity of historical climate simulations to uncertain aerosol forcing. *Geophys. Res. Lett.*, **47**, e2019GL085806, https://doi.org/10.1029/2019GL085806.

Dong, B., R. T. Sutton, E. Highwood, and L. Wilcox, 2014: The impacts of European and Asian anthropogenic sulfur dioxide emissions on Sahel rainfall. *J. Climate*, **27**, 7000–7017, https://doi.org/10.1175/JCLI-D-13-00769.1.

Dong, Y., C. Proistosescu, K. C. Armour, and D. S. Battisti, 2019: Attributing historical and future evolution of radiative feedbacks to regional warming patterns using a Green's function approach: The preeminence of the western Pacific. *J. Climate*, **32**, 5471–5491, https://doi.org/10.1175/JCLI-D-18-0843.1.

Fischer, E., and R. Knutti, 2015: Anthropogenic contribution to global occurrence of heavy-precipitation and high-temperature extremes. *Nat. Climate Change*, **5**, 560–564, https://doi.org/10.1038/nclimate2617.

Friedman, A. R., Y. Hwang, J. C. H. Chiang, and D. M. W. Frierson, 2013: Interhemispheric temperature asymmetry over the twentieth century and in future projections. *J. Climate*, **26**, 5419–5433, https://doi.org/10.1175/JCLI-D-12-00525.1.

——, G. C. Hegerl, A. P. Schurer, S. Lee, W. Kong, W. Cheng, and J. C. H. Chiang, 2020: Forced and unforced decadal behavior of the interhemispheric SST contrast during the instrumental period (1881–2012): Contextualizing the late 1960s–early 1970s shift. *J. Climate*, **33**, 3487–3509, https://doi.org/10.1175/JCLI-D-19-0102.1.

Ganguly, D., P. J. Rasch, H. Wang, and J.-H. Yoon, 2012: Climate response of the South Asian monsoon system to anthropogenic aerosols. *J. Geophys. Res.*, **117**, D13209, https://doi.org/10.1029/2012JD017508.

Gettelman, A., and Coauthors, 2010: Global simulations of ice nucleation and ice supersaturation with an improved cloud scheme in the Community Atmosphere Model. *J. Geophys. Res.*, **115**, D18216, https://doi.org/10.1029/2009JD013797.

——, L. Lin, B. Medeiros, and J. Olson, 2016: Climate feedback variance and the interaction of aerosol forcing and feedbacks. *J. Climate*, **29**, 6659–6675, https://doi.org/10.1175/JCLI-D-16-0151.1.

Ghan, S., and Coauthors, 2016: Challenges in constraining anthropogenic aerosol effects on cloud radiative forcing using present-day spatiotemporal variability. *Proc. Natl. Acad. Sci. USA*, **113**, 5804–5811, https://doi.org/10.1073/pnas.1514036113.

Giannini, A., and A. Kaplan, 2019: The role of aerosols and greenhouse gases in Sahel drought and recovery. *Climatic Change*, **152**, 449–466, https://doi.org/10.1007/s10584-018-2341-9.

Gryspeerdt, E., and Coauthors, 2020: Surprising similarities in model and observational aerosol radiative forcing estimates. *Atmos. Chem. Phys.*, **20**, 613–623, https://doi.org/10.5194/acp-20-613-2020.

Hawkins, E., and R. Sutton, 2009: The potential to narrow uncertainty in regional climate predictions. *Bull. Amer. Meteor. Soc.*, **90**, 1095–1108, https://doi.org/10.1175/2009BAMS2607.1.

Haywood, J. M., A. Jones, N. Bellouin, and D. Stephenson, 2013: Asymmetric forcing from stratospheric aerosols impacts Sahelian rainfall. *Nat. Climate Change*, **3**, 660–665, https://doi.org/10.1038/nclimate1857.

Hegerl, G. C., H. von Storch, K. Hasselmann, B. D. Santer, U. Cubasch, and P. D. Jones, 1996: Detecting greenhouse-gas-induced climate change with an optimal fingerprint method. *J. Climate*, **9**, 2281–2306, https://doi.org/10.1175/1520-0442(1996)009<2281:DGGICC>2.0.CO;2.

Held, I. M., and B. J. Soden, 2006: Robust responses of the hydrological cycle to global warming. *J. Climate*, **19**, 5686–5699, https://doi.org/10.1175/JCLI3990.1.

Huang, B., and Coauthors, 2017: Extended Reconstructed Sea Surface Temperature, version 5 (ERSSTv5): Upgrades, validations, and intercomparisons. *J. Climate*, **30**, 8179–8205, https://doi.org/10.1175/JCLI-D-16-0836.1.

Hwang, Y. T., D. M. Frierson, and S. M. Kang, 2013: Anthropogenic sulfate aerosol and the southward shift of tropical precipitation in the late 20th century. *Geophys. Res. Lett.*, **40**, 2845–2850, https://doi.org/10.1002/grl.50502.

Jiménez-de-la-Cuesta, D., and T. Mauritsen, 2009: Emergent constraints on Earth's transient and equilibrium response to doubled CO_2 from post-1970s global warming. *Nat. Geosci.*, **12**, 902–905, https://doi.org/10.1038/s41561-019-0463-y.

Kang, S. M., Y. Shin, and S.-P. Xie, 2018: Extratropical forcing and tropical rainfall distribution: Energetics framework and ocean Ekman advection. *npj Climate Atmos. Sci.*, **1**, 20172, https://doi.org/10.1038/s41612-017-0004-6.

——, and Coauthors, 2019: Extratropical–Tropical Interaction Model Intercomparison Project (ETIN-MIP): Protocol and initial results. *Bull. Amer. Meteor. Soc.*, **100**, 2589–2606, https://doi.org/10.1175/BAMS-D-18-0301.1.

Kay, J. E., and Coauthors, 2015: The Community Earth System Model (CESM) large ensemble project: A community resource for studying climate change in the presence of internal climate variability. *Bull. Amer. Meteor. Soc.*, **96**, 1333–1349, https://doi.org/10.1175/BAMS-D-13-00255.1.

Lamarque, J.-F., and Coauthors, 2010: Historical (1850–2000) gridded anthropogenic and biomass burning emissions of reactive gases and aerosols: Methodology and application. *Atmos. Chem. Phys.*, **10**, 7017–7039, https://doi.org/10.5194/acp-10-7017-2010.

Lehner, F., C. Deser, N. Maher, J. Marotzke, E. Fischer, L. Brunner, R. Knutti, and E. Hawkins, 2020: Partitioning climate projection uncertainty with multiple large ensembles and CMIP5/6. *Earth Syst. Dyn.*, **11**, 491–508, https://doi.org/10.5194/esd-11-491-2020.

Li, X., M. Ting, and D. E. Lee, 2018: Fast adjustments of the Asian summer monsoon to anthropogenic aerosols. *Geophys. Res. Lett.*, **45**, 1001–1010, https://doi.org/10.1002/2017GL076667.

Liu, X., and Coauthors, 2012: Toward a minimal representation of aerosols in climate models: Description and evaluation in the Community Atmosphere Model CAM5. *Geosci. Model Dev.*, **5**, 709–739, https://doi.org/10.5194/gmd-5-709-2012.

Maher, N., and Coauthors, 2019: The Max Planck Institute Grand Ensemble: Enabling the exploration of climate system variability. *J. Adv. Model. Earth Syst.*, **11**, 2050–2069, https://doi.org/10.1029/2019MS001639.

Manabe, S., and R. Stouffer, 1993: Century-scale effects of increased atmospheric CO_2 on the ocean–atmosphere system. *Nature*, **364**, 215–218, https://doi.org/10.1038/364215a0.

McKinnon, K. A., and C. Deser, 2018: Internal variability and regional climate trends in an observational large ensemble. *J. Climate*, **31**, 6783–6802, https://doi.org/10.1175/JCLI-D-17-0901.1.

——, A. Poppick, E. Dunn-Sigouin, and C. Deser, 2017: An "observational large ensemble" to compare observed and modeled temperature trend uncertainty due to internal variability. *J. Climate*, **30**, 7585–7598, https://doi.org/10.1175/JCLI-D-16-0905.1.

Milinski, S., N. Maher, and D. Olonscheck, 2019: How large does a large ensemble need to be? *Earth Syst. Dyn. Discuss.*, https://doi.org/10.5194/esd-2019-70.

Ming, Y., and V. Ramaswamy, 2009: Nonlinear climate and hydrological responses to aerosol effects. *J. Climate*, **22**, 1329–1339, https://doi.org/10.1175/2008JCLI2362.1.

Morrison, H., and A. Gettelman, 2008: A new two-moment bulk stratiform cloud microphysics scheme in the NCAR Community Atmosphere Model (CAM3), Part I: Description and numerical tests. *J. Climate*, **21**, 3642–3659, https://doi.org/10.1175/2008JCLI2105.1.

Myhre, G., and Coauthors, 2013: Anthropogenic and natural radiative forcing. *Climate Change 2013: The Physical Science Basis*, T. F. Stocker et al., Eds., Cambridge University Press, 659–740.

——, and Coauthors, 2017: PDRMIP: A precipitation driver and response model intercomparison project—Protocol and preliminary results. *Bull. Amer. Meteor. Soc.*, **98**, 1185–1198, https://doi.org/10.1175/BAMS-D-16-0019.1.

Neale, R. B., and Coauthors, 2012: Description of the NCAR Community Atmosphere Model (CAM 5.0). NCAR Tech. Note NCAR/TN-486+STR, 268 pp., https://doi.org/10.5065/D6N877R0.

Neelin, J. D., C. Chou, and H. Su, 2003: Tropical drought regions in global warming and El Niño teleconnections. *Geophys. Res. Lett.*, **30**, 2275, https://doi.org/10.1029/2003GL018625.

Pendergrass, A. G., F. Lehner, B. M. Sanderson, and Y. Xu, 2015: Does extreme precipitation intensity depend on the emissions scenario? *Geophys. Res. Lett.*, **42**, 8767–8774, https://doi.org/10.1002/2015GL065854.

Persad, G. G., and K. Caldeira, 2018: Divergent global-scale temperature effects from identical aerosols emitted in different regions. *Nat. Commun.*, **9**, 3289, https://doi.org/10.1038/s41467-018-05838-6.

Rayner, N. A., D. E. Parker, E. B. Horton, C. K. Folland, L. V. Alexander, D. P. Rowell, E. C. Kent, and A. Kaplan, 2003: Global analyses of sea surface temperature, sea ice, and night marine air temperature since the late nineteenth century. *J. Geophys. Res.*, **108**, 4407, https://doi.org/10.1029/2002JD002670.

Rohde, R., and Coauthors, 2013: Berkeley Earth temperature averaging process. *Geoinfor. Geostat.: Overview*, **1**, 20–100, https://doi.org/10.4172/2327-4581.1000103.

Rotstayn, L. D., and U. Lohmann, 2002: Tropical rainfall trends and the indirect aerosol effect. *J. Climate*, **15**, 2103–2116, https://doi.org/10.1175/1520-0442(2002)015<2103:TRTATI>2.0.CO;2.

Samset, B. H., M. T. Lund, M. Bollasina, G. Myhre, and L. Wilcox, 2019: Emerging Asian aerosol patterns. *Nat. Geosci.*, **12**, 582–584, https://doi.org/10.1038/s41561-019-0424-5.

Santer, B., J. C. Fyfe, S. Solomon, J. F. Painter, C. Bonfils, G. Pallotta, and M. D. Zelinka, 2019: Quantifying stochastic uncertainty in detection time of human-caused climate signals. *Proc. Natl. Acad. Sci.*, **116**, 19 821–19 827, https://doi.org/10.1073/pnas.1904586116.

Schneider, U., A. Becker, P. Finger, A. Meyer-Christoffer, B. Rudolf, and M. Ziese, 2015: GPCC full data reanalysis version 6.0 at 0.5°: Monthly land-surface precipitation from rain-gauges built on GTS-based and historic data. Global Precipitation Climatology Centre, accessed October 2019, https://doi.org/10.5676/DWD_GPCC/FD_M_V7_050.

Seo, J., S. M. Kang, and D. M. Frierson, 2014: Sensitivity of intertropical convergence zone movement to the latitudinal position of thermal forcing. *J. Climate*, **27**, 3035–3042, https://doi.org/10.1175/JCLI-D-13-00691.1.

Sippel, S., N. Meinshausen, A. Merrifield, F. Lehner, A. G. Pendergrass, E. Fischer, and R. Knutti, 2019: Uncovering the forced climate response from a single ensemble member using statistical learning. *J. Climate*, **32**, 5677–5699, https://doi.org/10.1175/JCLI-D-18-0882.1.

Soden, B., and E. Chung, 2017: The large-scale dynamical response of clouds to aerosol forcing. *J. Climate*, **30**, 8783–8794, https://doi.org/10.1175/JCLI-D-17-0050.1.

Solomon, A., L. M. Polvani, K. L. Smith, and R. P. Abernathey, 2015: The impact of ozone depleting substances on the circulation, temperature, and salinity of the Southern Ocean: An attribution study with CESM1(WACCM). *Geophys. Res. Lett.*, **42**, 5547–5555, https://doi.org/10.1002/2015GL064744.

Stevens, B., 2015: Rethinking the lower bound on aerosol radiative forcing. *J. Climate*, **28**, 4794–4819, https://doi.org/10.1175/JCLI-D-14-00656.1.

Stevenson, S., A. Capotondi, J. Fasullo, and B. Otto-Bliesner, 2019: Forced changes to twentieth century ENSO diversity in a last millennium context. *Climate Dyn.*, **52**, 7359–7374, https://doi.org/10.1007/s00382-017-3573-5.

Stuecker, M. F., and Coauthors, 2020: Strong remote control of future equatorial warming by off-equatorial forcing. *Nat. Climate Change*, **10**, 124–129, https://doi.org/10.1038/s41558-019-0667-6.

Swart, N. C., and Coauthors, 2019: The Canadian Earth System Model version 5 (CanESM5.0.3). *Geosci. Model Dev.*, **12**, 4823–4873, https://doi.org/10.5194/gmd-12-4823-2019.

Taylor, K. E., R. J. Stouffer, and G. A. Meehl, 2012: An overview of CMIP5 and the experiment design. *Bull. Amer. Meteor. Soc.*, **93**, 485–498, https://doi.org/10.1175/BAMS-D-11-00094.1.

Tebaldi, C., and J. M. Arblaster, 2014: Pattern scaling: Its strengths and limitations, and an update on the latest model simulations. *Climatic Change*, **122**, 459–471, https://doi.org/10.1007/s10584-013-1032-9.

Thompson, D. W. J., E. A. Barnes, C. Deser, W. E. Foust, and A. S. Phillips, 2015: Quantifying the role of internal climate variability in future climate trends. *J. Climate*, **28**, 6443–6456, https://doi.org/10.1175/JCLI-D-14-00830.1.

Ting, M., Y. Kushnir, R. Seager, and C. Li, 2009: Forced and internal twentieth-century SST trends in the North Atlantic. *J. Climate*, **22**, 1469–1481, https://doi.org/10.1175/2008JCLI2561.1.

Tomas, R. A., C. Deser, and L. Sun, 2016: The role of ocean heat transport in the global climate response to projected Arctic sea ice loss. *J. Climate*, **29**, 6841–6859, https://doi.org/10.1175/JCLI-D-15-0651.1.

Undorf, S., D. Polson, M. A. Bollasina, Y. Ming, A. Schurer, and G. C. Hegerl, 2018a: Detectable impact of local and remote anthropogenic aerosols on the 20th century changes of West African and South Asian monsoon precipitation. *J. Geophys. Res. Atmos.*, **123**, 4871–4889, https://doi.org/10.1029/2017jd027711.

——, M. A. Bollasina, and G. C. Hegerl, 2018b: Impacts of the 1900–1974 increase in anthropogenic aerosol emissions from North America and Europe on Eurasian summer climate. *J. Climate*, **31**, 8381–8399, https://doi.org/10.1175/JCLI-D-17-0850.1.

van Marle, M. J. E., and Coauthors, 2017: Historic global biomass burning emissions for CMIP6 (BB4CMIP) based on merging satellite observations with proxies and fire models (1750–2015). *Geosci. Model Dev.*, **10**, 3329–3357, https://doi.org/10.5194/gmd-10-3329-2017.

Wang, C.-C., W.-L. Lee and C. Chou, 2019: Climate effects of anthropogenic aerosol forcing on tropical precipitation and circulations. *J. Climate*, **32**, 5275–5287, https://doi.org/10.1175/JCLI-D-18-0641.1.

Wang, H., S. Xie, and Q. Liu, 2016: Comparison of climate response to anthropogenic aerosol versus greenhouse gas forcing: Distinct patterns. *J. Climate*, **29**, 5175–5188, https://doi.org/10.1175/JCLI-D-16-0106.1.

Wang, K., C. Deser, L. Sun, and R. A. Tomas, 2018: Fast response of the tropics to an abrupt loss of Arctic sea ice via ocean dynamics. *Geophys. Res. Lett.*, **45**, 4264–4272, https://doi.org/10.1029/2018gl077325.

White, R. H., A. A. McFarlane, D. M. W. Frierson, S. M. Kang, Y. Shin, and M. Friedman, 2018: Tropical precipitation and cross-equatorial heat transport in response to localized heating: Basin and hemisphere dependence. *Geophys. Res. Lett.*, **45**, 11 949–11 958, https://doi.org/10.1029/2018GL078781.

Wilcox, L. J., E. J. Highwood, B. B. B. Booth, and K. S. Carslaw, 2015: Quantifying sources of inter-model diversity in the cloud albedo effect. *Geophys. Res. Lett.*, **42**, 1568–1575, https://doi.org/10.1002/2015GL063301.

——, and Coauthors, 2020: Accelerated increases in global and Asian summer monsoon precipitation from future aerosol reductions. *Atmos. Chem. Phys. Discuss.*, https://doi.org/10.5194/acp-2019-1188.

Wills, R. C. J., D. S. Battisti, K. C. Armour, T. Schneider, and C. Deser, 2020: Pattern recognition methods to separate forced responses from internal variability in climate model ensembles and observations. *J. Climate*, https://doi.org/10.1175/JCLI-D-19-0855.1, in press.

Xie, S.-P., C. Deser, G. A. Vecchi, J. Ma, H. Teng, and A. T. Wittenberg, 2010: Global warming pattern formation: Sea surface temperature and rainfall. *J. Climate*, **23**, 966–986, https://doi.org/10.1175/2009JCLI3329.1.

——, B. Lu, and B. Xiang, 2013: Similar spatial patterns of climate responses to aerosol and greenhouse gas changes. *Nat. Geosci.*, **6**, 828–832, https://doi.org/10.1038/ngeo1931.

Xu, Y., J. Lamarque, and B. M. Sanderson, 2018: The importance of aerosol scenarios in projections of future heat extremes. *Climatic Change*, **146**, 393–406, https://doi.org/10.1007/s10584-015-1565-1.

Yeager, S. G., and Coauthors, 2018: Predicting near-term changes in the Earth system: A large ensemble of initialized decadal prediction simulations using the Community Earth System Model. *Bull. Amer. Meteor. Soc.*, **99**, 1867–1886, https://doi.org/10.1175/BAMS-D-17-0098.1.

Zelinka, M. D., T. Andrews, P. M. Forster, and K. E. Taylor, 2014: Quantifying components of aerosol–cloud–radiation interactions in climate models. *J. Geophys. Res. Atmos.*, **119**, 7599–7615, https://doi.org/10.1002/2014jd021710.

Zhao, A., D. S. Stevenson, and M. A. Bollasina, 2019: Climate forcing and response to greenhouse gases, aerosols, and ozone in CESM1. *J. Geophys. Res. Atmos.*, **124**, 13 876–13 894, https://doi.org/10.1029/2019JD030769.